TIDALLY DRIVEN DYNAMICS IN BONNE BAY, NEWFOUNDLAND

WENJUN PENG

Tidally Driven Dynamics in Bonne Bay, Newfoundland

by

©Wenjun Peng
B.Sc. (2005) Ocean University of China

A thesis submitted to the
School of Graduate Studies
in partial fulfillment of the
requirement for the degree of
Master of Science

Environmental Science Graduate Program
Memorial University of Newfoundland
January 2008

St. John's Newfoundland

Contents

Abstract

A suite of observations from May 2006 to March 2007 is used to describe the vertical structure and temporal variations of currents and hydrography on the sill of East Arm of Bonne Bay, Newfoundland. The instruments include a moored ADCP, multiple-frequency BioSonics echo-sounders, and a fixed hydrographic package with CTDs and an *ECO* fluorometer. These observations provide a detailed description of circulation at different timescales and reveals that the tide is the dominant forcing over the sill. The M_2 tide is the most energetic tidal constituent and contributes roughly 70% of the total tidal kinetic energy. The M_2 baroclinic tide is detected only in summer when stratification is strong. It has a wavelength of 7 km and has an energy that is about 20% of the barotropic kinetic energy. The subtidal current over the sill has a fortnightly modulation associated with spring-neap cycles between late September and November 2006, which indicates that deep-water renewal is not controlled by wind forcing but rather by changes in the horizontal stratification due to variations in tidal amplitudes. High-frequency internal waves with period of 80 minutes are identified in the data from ADCP and BioSonics echo-sounders in summer, 2006. They display asymmetry during tidal cycles: the wave structure only develops on the ebb tide, and the amplitude is 3 m and group velocity is 35 cm/s. It has about 1% of the barotropic kinetic energy. The high-frequency internal waves are generated near the side of the inner basin and propagate towards the outer area.

Acknowledgements

I would like to thank my supervisor, Dr. Brad deYoung, for giving me this opportunity to study in Memorial University, also for his guidance and help with my study and research. I appreciate the funding from both Brad and the School of Graduate Studies during this master program.

I am grateful to Steven Stringer and Jack Foley, for their great patience in discussing with me about all my questions regarding the data and instruments from Bonne Bay Observatory. Additionally I want to thank Marina Blokhina for her advice on processing Biosonics data and internal waves in the beginning of my research. And also, I want to thank Len Zedel and Entcho Demirov, for their invaluable comments and suggestions as the thesis reviewers.

Finally, I would like to thank my parents and my friends, for their unconditional support throughout my study in Canada and always.

List of Tables

List of Figures

List of Abbreviations

ADCP – Acoustic Doppler current profiler

BBO – Bonne Bay Observatory

cpd – cycles per day

CTD – conductivity temperature depth

dB – decibels

kHz – kilohertz

pps – pings per second

PSD – Power Spectral Density

psu – practical salinity units

1 Introduction

Fjords are glacially carved embayments existing in mountainous coast at high latitudes such as Scandinavia and North America (Farmer and Freeland, 1983). A fjord is a type of estuary and the physical processes of circulation in these systems are both complex and interacting. The dynamics of fjords attracted oceanographers and led to their study for over a century with theoretical, modelling and observational approaches having been applied. This thesis will bring focus on the dynamics of Bonne Bay, a natural fjord on the west coast of Newfoundland, Canada and illustrate some important physical processes occurring over the sill of the fjord. We will use observations collected as part of ongoing studies in support of the Bonne Bay Ocean Observatory (deYoung et al. 2005)

1.1 Study Area, Bonne Bay

Bonne Bay is a natural fjord within Gros Morne National Park on the west coast of Newfoundland (Figure 1.1). It is located roughly midway between Cape Ray to the southwest and the Strait of Belle Isle to the northeast. It consists of two basins, one of which is much larger and deeper than the other. The inner basin, called East Arm, is about 12 km long, has a maximum depth of 230 m, and is separated from the outer basin by a 15 m deep sill, which is a ridge above the average bottom level in a fjord and separates one basin from the outer area. The outer basin is about 30 km long and has a maximum depth of 140 m. There is no true sill associated with this basin. It includes South Arm, and extends roughly 15 to 20 km beyond the coastline to the Gulf of St. Lawrence (Gilbert et al. 1993).

Bonne Bay has the typical fjord structure, long and narrow, and with steep sides and cliffs, deeper interiors than coastal shelf. The Long Range Mountains, which are about 500 km in length and 500 m to 800 m in height, surround Bonne Bay aligned in a SSW-NNE direction. The Tablelands, a plateau of uplifted ocean crust, are located to the southwest. They guide the near surface winds, resulting in a strong southwesterly wind which is the mean wind direction everywhere into the island during the summer on west Newfoundland. To the north of Bonne Bay, the steep cliffs of the Long Range Mountains guide the alongshore coastal winds (Gilbert and Pettigrew, 1993).

The Gulf of St. Lawrence is a stratified semi-enclosed sea and connects the bay with the Atlantic Ocean through the Cabot Strait and the Straits of Belle Isle. Bonne Bay is an estuary system and the circulation is characterized by salty inflow of ocean water in the deeper layer and an outflow of brackish water on the surface toward the ocean. Estuaries are physically complicated and ecologically important and the study of circulation and flow in estuaries is important to many branches of oceanography (Farmer and Freeland, 1983).

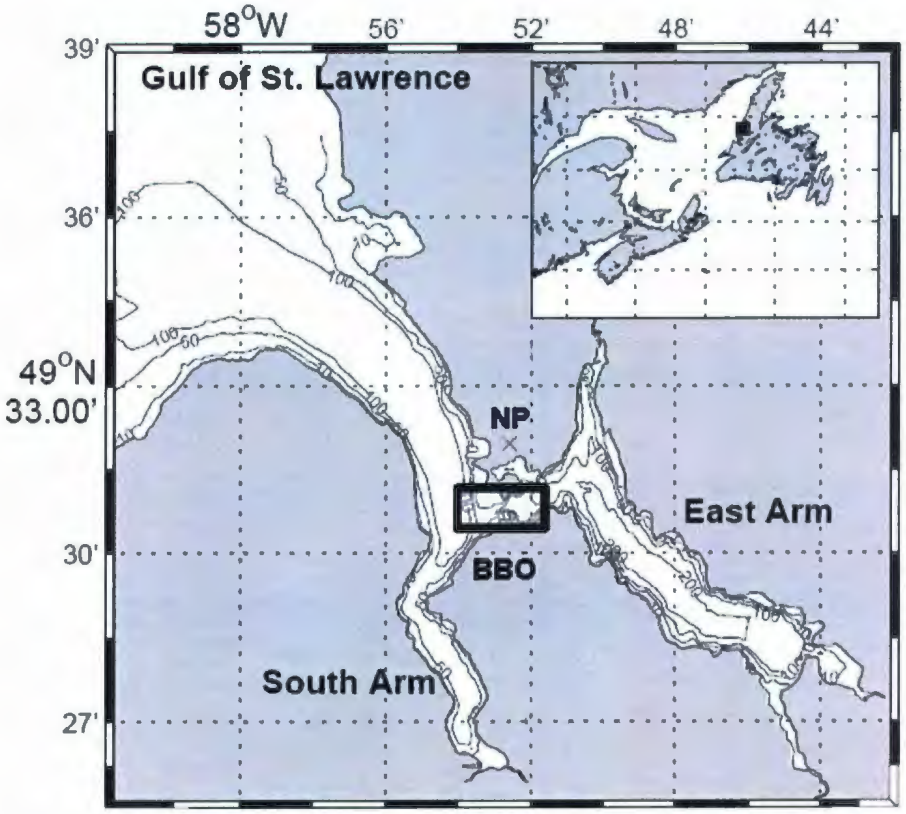

Figure 1.1: Bathymetry and location of Bonne Bay on west coast of Newfoundland, Canada. NP is the Norris Point weather station and BBO is the Bonne Bay Observatory. Contour interval is 10 meters.

1.2 Estuary and Fjord Basics

An estuary is defined as "a semi-enclosed coastal body of water having a free connection to the open sea and within which the sea-water is measurably diluted with fresh water deriving from land drainage" (Pickard et al. 1990). The river water from land mix with salt water and eventually flows out to the open sea and a corresponding inflow

of seawater occurs below it. One can consider a steady-state description of the flow dynamics to represent the average characteristics of a fjord.

Cameron and Pritchard (1963) categorized estuaries based on stratification and salinity. According to their category, fjords belong to *highly stratified estuaries* with freshwater input and a submarine sill which separates them from the outer ocean. The inland end where rivers empty into the fjord is called the head and the seaward end the mouth. They are usually long relative to their width and have an almost rectangular cross-section with steep sides and sharp bends (Farmer and Freeland, 1983). The sea floor of a fjord is generally rocky or having very thin layers of sediment. Deposition normally happens at the head where river runoff enters (Dyer 1997).

Most fjords have a surface layer with almost constant thickness along the length. Both temperature and salinity profiles commonly demonstrate a two-layer system with a significant vertical gradient in the surface layer and roughly constant values in the deep layer (except over the sill). Sill is shallower than both the inner basin of fjord and the outer sea and restricts the exchange of deep water (Dyer 1997).

1.3 Fjord Process

The circulation of coastal water differs in many aspects from the open ocean: variations of water properties and dynamics in coastal area are larger due to the presence of the coast as a boundary to flow, shallowness of the water on the continental shelf, the presence of river runoff, precipitation and anthropogenic factors, e.g. sewage disposal and industrial effluent (Pickard et al. 1990). These different factors interact to influence the circulation and dynamics of the fjord. Most estuaries exhibit a two-layer flow in a

time-averaged sense, with outflow of brackish water in the surface and inflow of dense water in the deep layer. The height between two layers in the water column in most estuaries where the mean flow is zero is called the *level of no motion* that occurs at the depth of the maximum vertical density gradient (Figure 1.2). Velocities in the lower layer are usually smaller then those in the upper layer due to the sill. Timescales for the exchange of the water in the inner basin of fjords can be from days to months (deYoung and Pond, 1988).

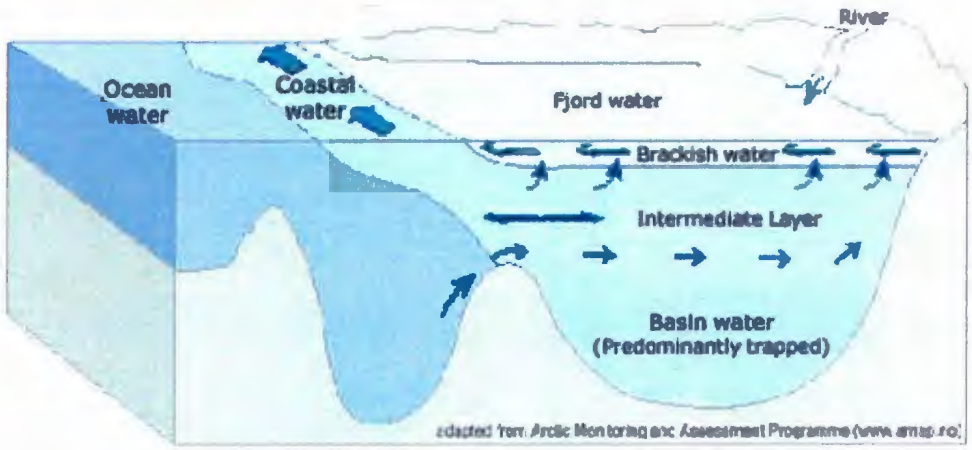

Figure 1.2: Schematic diagram of a fjord circulation, showing that the exchange of ocean and basin water through the sill with the salty ocean water in the deeper layer and brackish water in the upper layer, and freshwater from the land drainage. (http://bbo.physics.mun.ca/background/why.php)

The exchange of fjord water with the outer ocean water is influenced by many mechanisms: tides force a cyclic renewal over the sill; freshwater runoff generate

horizontal density gradients across the sill and drive the dense inflow with wind forcing; and shelf process drives the dense water up to the height of sill and the gravitational circulation (Farmer and Freeland, 1983). The dense water raised above the height of the sill can propagate into the inner basin of fjords as a density current and then cause the exchange process, which are demonstrated by sharp changes both in density and temperature of the water in a fjord (deYoung and Pond, 1988).

1.3.1 Tides

In fjords, barotropic tides are generally the most energetic components to fjord circulations. Tides promote turbulence and then vertical mixing, and thus break down the stratification of the water and generate the mean flow, and effect the gravitational circulation and deep water renewal (Farmer and Freeland, 1983): salt water can be renewed by flood tide and recedes during the ebb, corresponding to the rise and fall of the density interface at tidal frequencies. Tidal velocities over a sill are larger because of topographic narrow, mixing is therefore stronger and the stratification weaker than those within the fjord.

Internal tides are the internal waves at the tidal frequencies. Theoretically the stratified fluid forced by the barotropic flow interacting with the sills results in the baroclinic tide. It is also observed that the position of isopycnal surfaces in a fjord oscillates at tidal frequencies, which indicates the existence of internal tides (Farmer and Freeland, 1983). Similar to barotropic tides, breaking of baroclinic tides can also supply energy to turbulence and mixing.

The questions also arise about how tides propagate and whether they are reflected or not. Normally the external Rossby radius (50-200 km) is much larger than typical fjord width (1-5 km), therefore, both the barotropic and first mode baroclinic tides in fjords propagate as a plane wave and most energy of the tides focuses on the component of along channel direction (Stigebrandt 1999). If the energy of the tides is dissipated by friction completely without reflection, or if the channel is too long to generate reflection, the tidal wave is called a *progressive wave.* Otherwise, the tidal waves travel to the head and then are reflected back, which is called a *standing wave.* In fjords, tidal wave is usually a mixture of both kinds of waves and can be reflected at the head (Dyer 1997).

1.3.2 River Discharge

River runoff can reduce the salinity of the surface layer of the water and change stratification. The seasonal variations of river runoff give rise to seasonal fluctuations of salinity in coastal waters. In high latitude regions, e.g. Bonne Bay, rivers are mainly supplied by the water from snow or glaciers melting, therefore compared to that in winter, the river runoff increases in summer causing the decrease of salinity in the upper layer of the water, and salinity variations are evident seasonally responding to the river discharge. Farmer and Freeland (1983) have presented the temperature and salinity profiles for two stations in Knight Inlet, British Columbia, one near the head and the other one near the mouth. The profiles show that there is sharp stratification at both stations in the summer and a surface layer of uniform salinity at the head due to the high river discharge, whereas stratification is almost nonexistent in the winter at both stations as the freshwater input is low (Figure 1.3).

Freshwater runoff also influences the exchange of fjord water with the outer environment by generating a horizontal density gradient and accelerating the baroclinic tides to replace and mix water. Increased freshwater runoff enhances mixing but meanwhile it also increases the thickness of the surface layer. In extreme cases for a shallow sill, it is possible to block the inflow completely, and this becomes the obstacle to the exchange process.

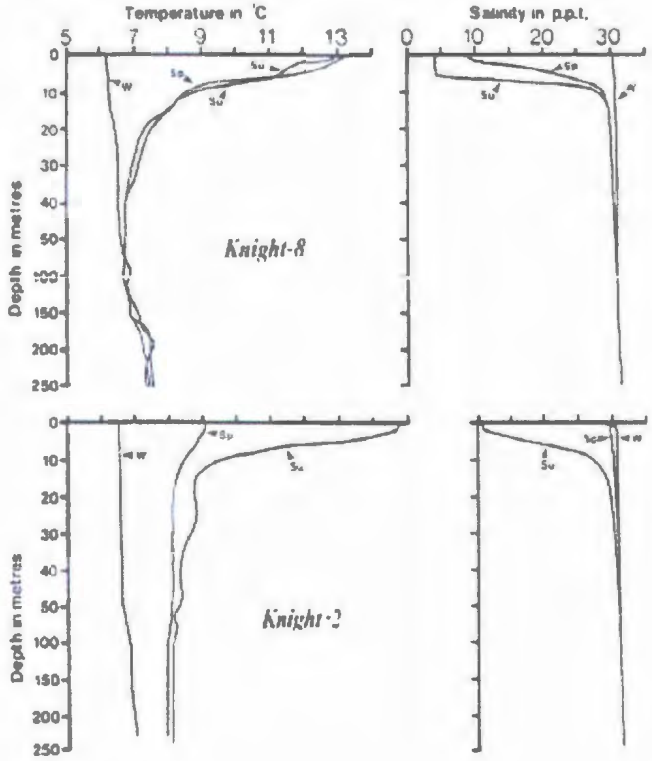

Figure 1.3: Temperature and salinity profiles of Knight Inlet in summer, spring and winter, Knight-8 near the head and Knight-2 near the mouth (Farmer and Freeland, 1983)

Much of the freshwater input to Bonne Bay is derived from the St. Lawrence Estuary (SLE) watershed and the northern shore rivers. Freshwater input to the GSL typically reaches a maximum of 32,370 m^3/s in May, and a minimum of 14,196 m^3/s in February (Richards, 2005). Both freshwater input and surface heat fluxes contribute to buoyancy forcing in the Bonne Bay fjord, with the formation of a strong stratification and a seasonal thermocline in summer, vertical mixing in autumn, and ice formation in winter. Sea ice generally forms in the middle of January, and melts in mid to late April.

1.3.3 Wind Forcing

Wind is another major source of energy in fjords in addition to tide. Wind can affect the fjord circulation by creating waves and additional mixing, and the effects have the time-scale of days to months. Wind stress is defined as drag force per unit area caused by wind shear. Wind stress at the sea surface applies a friction force that can drive ocean currents and generate turbulence for mixing and increase the potential energy of the water column (Farmer and Freeland, 1983). Klinck, O'Brien and Svendsen (1982) applied a numerical model of continental shelf driven by wind forcing to a fjord. They found that alongshore wind is more important to fjord/shelf exchange as it drives currents perpendicular to the shore in the surface Ekman layer with an offset flow in the deep layer, while an offshore wind can not cause the net change in the volume of the fjord water.

Fjords steer the direction of wind along the inlet by the high and steep sides of the coastline. Wind speed along the channel varies with the change of channel width; it decreases with the increasing width and also towards the interior. Moreover, the wind

effects on fjord water differ from those on currents in the deep ocean: the narrowness of fjords restricts rotation effects and inertial motions which are common in the deep ocean, and wind driven currents interact with fjord boundaries in contrast to no boundaries in the open ocean. Wind-driven surface current in the surface layer of fjords can cause the depth change of pycnocline, which is in the form of either standing waves or progressive waves (Farmer and Freeland, 1983).

1.4 Previous Research at Bonne Bay

The Bonne Bay Marine Station was built in Norris Point Waterfront in 2002 to study the unique marine ecosystem. Therefore, most of the research and papers about Bonne Bay so far have focused on marine biology and ecology, including diversity of habitat, population, distribution, and migration of marine plants, fish, invertebrates and other organisms (Ennis et al. 1990; Comeau et al. 1998; Tian et al. 2001).

Gilbert and Pettigrew conducted research on physical oceanography during the summer of 1991. With time series of hydrographic data and velocity components in the outer basin of the South Arm, they calculated the means and standard deviations and the main tidal constants, together with their corresponding low-passed time series. They explored the effects of wind on circulation and found that wind was a major impact on flows. Richards (2005) analyzed current meter data from Acoustic Doppler Current Profilers (ADCPs) deployed between September 2002 and September 2004 on the sill of the East Arm and hydrographic data around the sill in June 2004. He focused on the subtidal flows and found that wind was the dominant forcing for the low-frequency flows.

He also noted the presence of internal tides and high-frequency internal waves but did not explore the details associated with mechanisms of these flows.

1.5 Thesis Objects and Outline

The objective of this research is to investigate the temporal variability of circulation and exchange process over the sill in Bonne Bay, with a particular focus on the tidal-driven dynamics at different time scales. Some properties of the observed tidal-driven dynamics are determined using data sets from moored current meters and hydrographic instruments. Following this introduction chapter, Chapter 2 describes the instruments and data sets from Bonne Bay Observatory (BBO). Chapter 3 gives the preliminary analysis of the data and presents the basic circulations over the sill. Chapter 4 discusses the tidal flow including properties of barotropic and baroclinic tides. The low-frequency circulations associated with the deep-water renewal, and high-frequency internal waves are examined in Chapter 5. Chapter 6 provides a brief summary and presents the conclusions.

2 Instruments and Data Information

An ocean observatory has been deployed at the bottom of a sill, at around 15 m water depth in Bonne Bay (Figure 2.1) to provide data on the physical environment and its influence on marine ecosystems. There are two basic ways to measure the currents in the ocean; the Eulerian method describes changes as they occur at a fixed point in the fluid, and the Lagrangian method considers changes which occur as you follow a fluid particle trajectory (Pickard et al. 1990). The observatory is fixed at the bottom of the sill and therefore provides Eulerian data that can be used to study the temporal variability of the water column above it on the sill.

Bonne Bay is ice-covered for three to four months of the year, and the underwater observatory will provide real-time data continuously in an ice-covered system that people previously only were able to sample intermittently. The essential parts of the Bonne Bay Observatory (BBO) system are oceanographic facilities, including video, acoustic and hydrographic instruments and the controlling hardware that supports them (Figure 2.2). Video instruments record both live video of the ocean and capture images of biological matter. Acoustic instruments include direct sound recording as well as acoustic sounder and current meter systems. Hydrographic instruments measure water properties such as temperature, salinity, fluorescence, oxygen and nitrogen levels, etc. (deYoung et al. 2005). The data used for this thesis are from the Acoustic Doppler current profiler (ADCP) and BioSonics DT-X echosounder of the acoustic instruments, Conductivity

Temperature Depth (CTD) sensors and a fluorometer of the hydrographic instruments, and wind data from the Norris Point weather station in Bonne Bay.

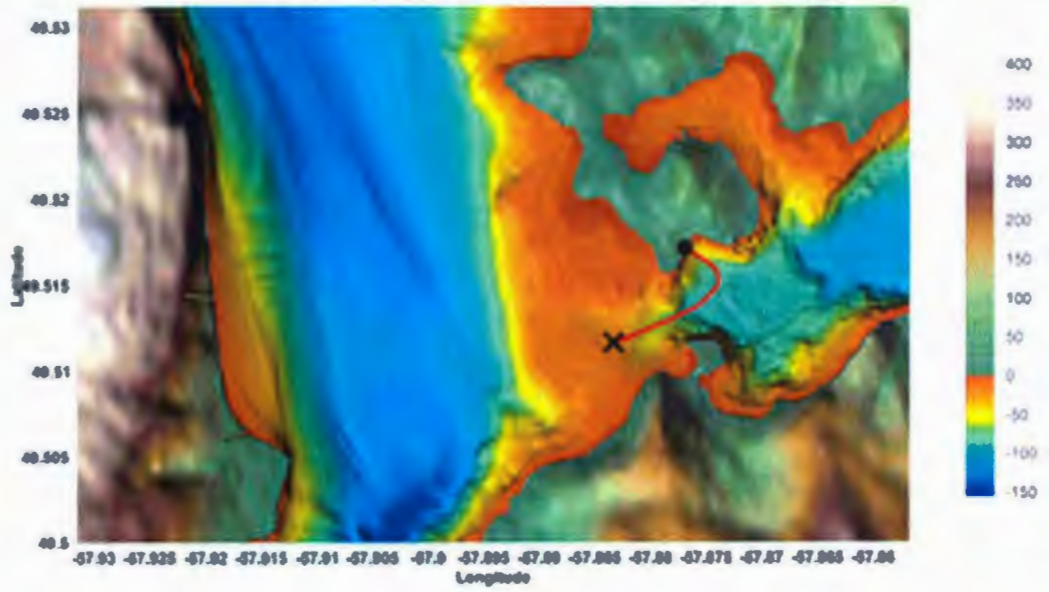

Figure 2.1: Position of Bonne Bay Observatory (denoted by the black X) over the sill. The red line is the underwater cable, connecting the observatory to the shore and providing both power and data communication. The shallow sill (orange) separates the deep outer bay (blue on the left) from the East Arm (aquamarine on the right) (http://bbo.physics.mun.ca/background/where.php).

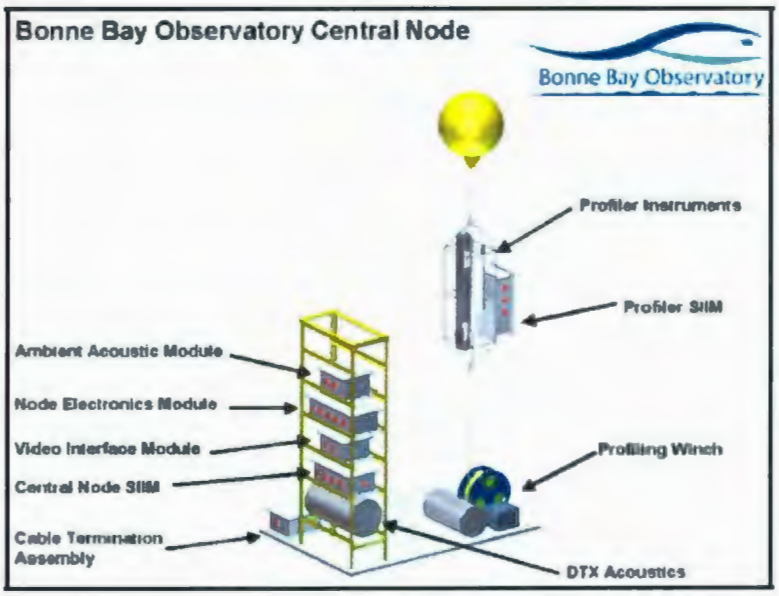

Figure 2.2: BBO central node configuration (deYoung et al. 2005).

2.1 ADCP Data

2.1.1 ADCP Basics

ADCPs measure both horizontal and vertical ocean velocities using the Doppler effect of backscattered sound. Small particles and zooplankton in the ocean are sound scatters which are considered to be passive swimmers floating in the water and move at the same velocity as the water on average. An ADCP transducer transmits sound pulses at a fixed frequency at the speed of sound. Sound scatters in all directions in the water and only a small amount of energy will be reflected back which is Doppler shifted. By

measuring the Doppler shifted frequency of the returning echoes, the relative velocity between the particle and the transducer, V, can be determined by

$$F_d = 2F_s(V/C) \tag{2.1}$$

where F_d is the Doppler shift frequency, F_s is the frequency of the sound when everything is still, and C is the speed of sound (RD Instruments, 1996). To the ADCP which is still and moored at the bottom, the relative velocity between a particle and the transducer is just the velocity of the particle, and also the velocity of the water based on the assumption that particles move with the water.

A single transducer can only measure a single velocity component radial to the beam since angular motion change no distance between the source and receiver, and causes no Doppler shift. Therefore, an ADCP uses multiple beams pointed in different directions to obtain velocities in three dimensions. Usually an ADCP has four acoustic beams in a Janus configuration, but only three of them are required to calculate three dimensional velocities, and the fourth beam is used for obtaining an error velocity caused by inhomogeneous water, low backscatter and equipment problems. ADCPs are able to provide a profile of velocities of the entire water column by dividing the column into uniform bins and measuring the average velocity over the range of each bin (RD Instruments, 1996).

2.1.2 Instrument and Data

Three ADCPs were deployed at the bottom of the sill in Bonne Bay one after another to cover 3 different time series from May 2006 to March 2007. They were all

upward-looking, RDI 4 beam Workhorse Broadband instruments working at different frequencies and sampling rates, and record data in the format of earth coordinate, which means that velocity is converted into north, east and up components. With a temperature sensor, they also can measure time series of temperature at the bottom. The details of each ADCP are given in Table 2.1. Bin1mid is the distance between the bottom and the center of the first bin, which is the closest bin to the bottom. Ensemble averaging of pings can reduce the relatively large error in single-ping velocity estimates.

The ADCP data were extracted from the instrument and saved in Matlab workspace. The surface was located by identifying the depth of the most intense backscatter signal, and then the top 2 meters of records were discarded because they were suspicious data caused by surface reflection. Bad data points were eliminated by linear interpolation.

Table 2.1: Details of the three ADCP instruments deployed on the sill

Instrument	Frequency (kHz)	Time (mm/dd/yy)	Bin1mid (m)	Binsize (m)	Pings/ensemble	Averaging period
BB06_a	307.2	05/04/06-06/21/06	3	1	180	15 min
BB06_b	614.4	06/21/06-09/11/06	2	1	100	30 min
BB06_c	614.4	09/11/06-03/21/07	2	1	90	15 min

2.2 BioSonics Data

2.2.1 BioSonics Basics

Sound is an exceptional medium to investigate the ocean interior compared to other forms of radiation, such as light, since it suffers significantly lower attenuation and therefore can travel longer distances than light. High-frequency (above 20 kHz) acoustic scattering technique is a powerful tool for studying small-scale physical processes that occur in the ocean interior because the corresponding wavelengths are commensurate with the processes under investigation (Medwin et al. 2005).

Acoustic techniques have extensive applications in both marine and freshwater environments for underwater acoustic assessment and monitoring, including imaging small-scale physical process such as internal waves, bathymetry, biological research, habitat assessment, population dynamics and plant and sediment distribution, etc. (BioSonics Inc. 2002). It can provide synoptic information of the interior, whereas sampling marine organisms using nets is very limiting and results in dispersed distributions.

There are currently three types of hydroacoustic techniques widely used: single beam, dual -beam, and the split-beam echosounders. All of them have been used to provide direct *in situ* measurements of the target strength of individual organism, and also the abundance. In addition, the split-beam system has the advantage in its ability to provide target angular location and thus can obtain the information on fish behavior, such as fish swimming speed, location in the water column, and direction of travel as they pass through the beam (Ehrenberg et al. 1996). Split-beam systems significantly enhance the

tracking performance compared to data collected from single and dual-beam systems and are especially useful for fixed location acoustic studies.

The BioSonics DT-X echosounder used at BBO is an underwater moored, upward-looking system, which records the intensity of backscattered sound. The echosounder at BBO consists of three digital transducers with two different beam patterns and various frequencies, one split beam transducer of 120 kHz and two single beam transducers of 220 kHz and 440 kHz respectively (Figure 2.3). The transducers send acoustic pulses into the water and then receive echoes from targets in the water, and convert them to electrical signals, by means of which they give information on both the amount and size of scattering organisms in the water column above, and also on the physical characteristics of passing wave motions (Figure 2.4).

Figure 2.3: The BioSonics DT-X echosounder system (Satlantic Inc. 2006).

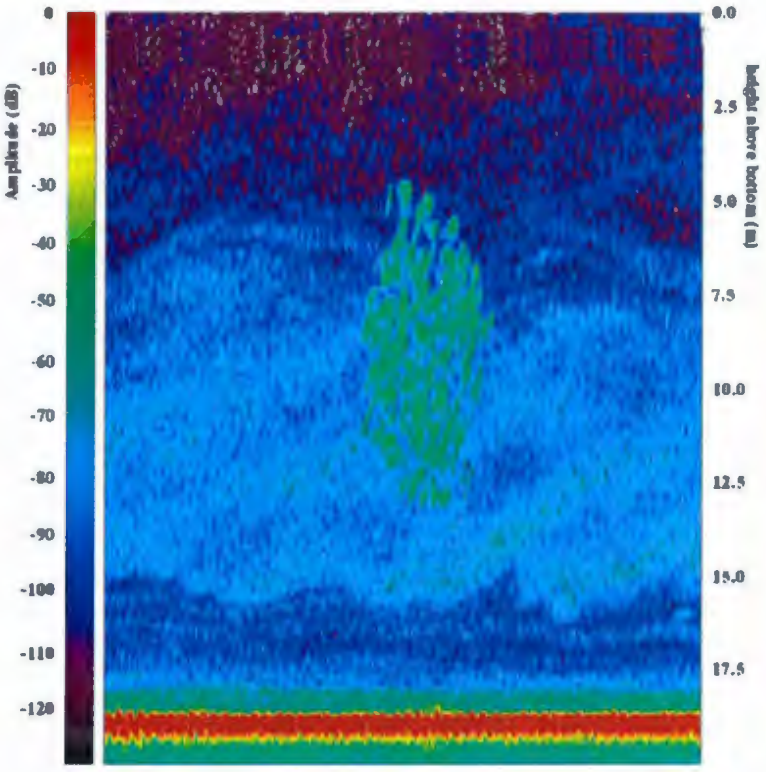

Figure 2.4: Inverted image of small school of fish (green patch) detected by the 120 kHz acoustic transducer in the water column. The orange line at the bottom is the sea surface (http://bbo.physics.mun.ca/data/acoustic.php).

2.2.2 Instrument Parameters

The operational parameters to a specific application are user-controlled and the key parameters consist of ping frequency, pulse duration, target strength level, range, threshold, etc. Range is the distance from the transducer to a certain depth within which the data are collected. Threshold level is the target strength level below which echo signal cannot be recorded. The pulse rate (ping frequency) and pulse duration are determined

according to the purpose why the data is being collected. For example, the typical value for detection of small fish might be 10 pps and 0.4 ms (BioSonics Inc. 2002). The three transducers of the BioSonics echosounder at BBO share the same values of a set of parameters for sampling, ping rate 0.1 pps, pulse duration 0.4 ms, threshold -130 dB, range around 25 m. The vertical water column is divided as 1383 uniform bins with the depth resolution around 2 cm. The transducer sends ping pulses to each bin at the same time and then receives returning echoes with the information at each depth.

2.2.3 Data Information

The raw data produced by the transducer of a DT-X echosounder is stored as .RTP and .NME files, and then automatically converted to .DT4 files for later use. .DT4 files contain binary data, and the Matlab scripts were created to read the binary data from the 3 transducers with different beam patterns and resave them into a Matlab format for analysis. The scripts are established based on the Matlab code, RDDTX.m from Rich Pawlowicz (http://www.eos.ubc.ca/~rich/), which only works for a single beam, single transducer. Since the DT-X echosounder deployed at Bonne Bay is mainly used to investigate the physical process over the sill, the angular information included in the files from the split-beam transducer has not been extracted. Therefore the meaningful output from all the three transducers is the volume backscattering strength Sv (in dB re m^{-1}). In the similar way as processing ADCP data, the surface was located by identifying at which depth the most intense backscatter signal occurred, and the suspicious data above the depth were discarded. Acoustic data are voluminous, in order to analyze longer time series of the BioSonics data, they were averaged in the vertical, with decreased depth

resolution about 5 cm, to cut down the total data volume. The time resolution is not changed, still 10 seconds per ping.

2.3 Hydrographic Data

The profiling package for obtaining hydrographic data in the Bonne Bay Observatory consists of a suite of instruments including two SBE-19*plus* SEACAT CTDs (sensors measuring ocean salinity, temperature, and pressure), a nitrate sensor, a *ECO* fluorometer (measuring fluorescence), a radiometer (measuring radiated light levels), and a gas tension sensor (measuring both oxygen and nitrogen levels). Unfortunately the package was not regularly developed up to the surface and retrieved back to measure the vertical profile of water properties during the sampling time, instead, it was fixed at the bottom of the sill all the time to obtain time series of water properties at the fixed point. Data from CTDs and the fluorometer will be analyzed and discussed in this thesis.

The raw data files from the CTDs were in text format, and then extracted and resaved into a Matlab workspace for analyzing. The output of SBE-19*plus* CTDs including conductivity, temperature, and pressure were used as the input to the 1978 Practical Salinity Scale Equations (Sea-Bird Electronics Inc. 2004) to calculate salinity values in units of psu. The density can be obtained using the equation of state based on salinity, temperature and pressure. In addition to the bottom CTD data from the observatory in 2006, there are vertical profiles of CTD data on both sides of the sill over several tidal cycles conducted by a cruise from June 9, 2004 to June 11, 2004. There is also one vertical sample over the sill (14 m) collected around 10:30 am on June 14, 2004 during the ebb tide, with sampling rate of 2 scans per second. The profiled data together

with the bottom hydrographic data from BBO were analyzed and the results will be shown in Chapter 3 to help understand the dynamics and exchange process over the sill during the tidal cycles.

Raw data from *ECO* fluorometer record chlorophyll concentrations in the water in units of counts, which was converted and expressed in μg/l according to the equation in the *ECO* Chlorophyll Fluorometer Characterization Sheet (an instrument-specific calibration sheet from the delivered Items),

$$CHL(\mu g / l) = SF * (Output - CWO) \tag{2.2}$$

where *CHL* is the chlorophyll concentration, *SF* is the scale factor, and *CWO* is the clean water offset (blank). The coefficients are provided in the calibration sheet; *SF* = 0.0078 μg/l/count, *CWO* = 120 counts. The missing data points from either CTD or fluorometer are linear interpolated.

2.4 Atmospheric Data

The wind data from May 2006 to March 2007 were obtained from the Bonne Bay weather station in Norris Point (Figure 1.1). It is nearby the observatory and the wind records there are a good representation of the local wind. The data files included speed and direction of local wind in the text format. Wind data were extracted and resaved in a Matlab format, and then separated into east-west and north-south components.

Wind stress transfers momentum flux to the ocean, and wind velocity is converted to wind stress according to the formulations following: at the surface of the ocean, the stress is proportional to the square of the wind velocity (Gill 1982),

$$\vec{\tau} = c_D \rho_a |\vec{u}| \vec{u} \tag{2.3}$$

where $\vec{\tau}$ is the wind stress, ρ_a is the air density at the sea level, the typical value of which is 1.25 kg/m^3, $\vec{u}$ is the wind velocity, and c_D is drag coefficient, a scaling term, the value of which only depends on the wind speed within 10 m height (Large and Pond, 1981).

$$c_D = 1.2 \times 10^{-3} \quad \text{for} \quad |\vec{u}| < 11 \text{ m/s} \tag{2.4}$$

$$10^3 c_D = 0.49 + 0.065 |\vec{u}| \quad \text{for} \quad |\vec{u}| \geq 11 \text{ cm/s} \tag{2.5}$$

3 Mean Characteristics of Circulation

In this chapter, ADCP and hydrographic data are preliminary analyzed to explore the basic circulation structure at different timescales over the sill. The hydrographic data were not continuously collected during the yearlong sampling period, with gaps from several days to months which cannot be eliminated by interpolation. These gaps in the data make them difficult to investigate. Some of the following analyses, therefore, will especially focus on the data from several different time periods within the sampling time which most kinds of data can cover.

3.1 Rotation Angles

To find the main orientation of fluid flow over the sill, principal component analysis was applied to the time series of ADCP data. The major and minor axes were determined by a covariance analysis. In this new coordinate system, most of the variance was along the alongshore axis and remaining along the cross-shore axis (Emery 1998). The rotation angle of the principle axis θ_p can be found by solving the eigenvalues of the covariance matrix for the u and v components,

$$\tan(2\theta_p) = \frac{\overline{2u'v'}}{\overline{u'^2} - \overline{v'^2}} \tag{3.1}$$

where $u' = u - \bar{u}$ and $v' = v - \bar{v}$. Then angles were used to rotate the u and v axes at each depth to obtain the alongshore and cross-shore velocity components. Figure 3.1 shows the rotation angles calculated from ADCP data at different time scales: the whole year and

three seasons. The four plots, although from different time periods, share the same features: the rotation angles vary with depth and the values are usually several degrees at each depth and change slightly with time. Richards (2004) also calculated the principle axes angles from ADCP data of 4 different moorings over the sill in the year 2002 and 2003. His results showed both depth dependence and location dependence for the rotation angles, with values varying from several degrees to a few decadegrees. In this thesis, the u and v components are not rotated due to the small values of the rotation angles, and east-west velocity through the water column above the mooring is assumed to be alongshore, and north-south velocity cross-shore.

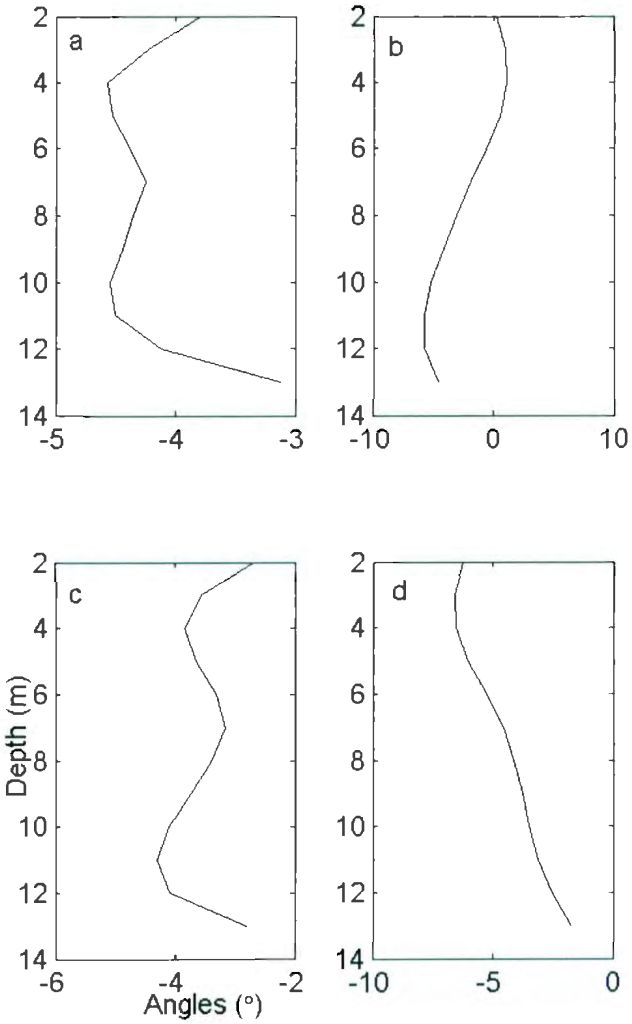

Figure 3.1: Rotation angles calculated at each depth for ADCP time series using a) the whole timeseries (from May 2006 to March 2007), b) summer data (from June to August), c) fall data (from September to November), and d) winter data (from December to February). Angles are given in degrees where 0^{o} is the East.

3.2 Basic Circulation

The ADCP velocity data, including u and v components, cover a nearly yearlong period from May 2006 to March 2007. It is also divided into three segment representing three seasons during the sampling time, summer from June to August, fall from September to November, and winter from December to the next February. Then the four different timeseries are averaged at each depth to investigate exchange process over the sill for both the yearlong and seasonal timescales.

Plots of mean velocities together with standard deviations are shown in Figure 3.2. The average horizontal alongshore velocities including yearlong and seasonal averages show the persistence of the estuary velocity and indicate a two-layer circulation system over the sill, a typical estuary scheme, with outflow in the upper layer, ranging from 6 to 13 cm/s at the surface, and inflow in the deeper layer with the comparable magnitude at the bottom. In addition, the average alongshore velocity is significantly depth dependent with the maximum outflow and inflow occurring at the surface and the bottom, respectively. There are also seasonal changes in average velocities. The averaged alongshore velocity in fall is larger than in winter, even though the fall and winter seasons have fairly close magnitudes, with the maximum outflow or inflow around 10 cm/s (Figure 3.3). Summer signals are weaker, with outflow velocity around 5 or 6 cm/s, half the value of the fall or winter maximum, which indicates that the exchange process over the sill is stronger during the fall and winter seasons than in summer. The alongshore velocity is greater than the cross-shore, by a factor of 5 to 10 in amplitude, which is fairly small as expected, with the average amplitude of 2 or 3 cm/s at all time

scales. Richards (2005) found similar results using the data from October 2003 to June 2004.

The *level of no motion*, corresponding to the zero alongshore velocity, is the boundary between the upper and lower layer in a two-layer estuary system. It is normally at the depth where the maximum vertical density gradient occurs, and can be affected by wind force and freshwater runoff. The temperature, density, and salinity plot using data from June 24, 2006 (Figure 3.4) demonstrates the depth of the interface, around 6 m in summer time, the same depth demonstrated by Figure 3.2b. However, the position is not consistent throughout a year and has monthly and seasonal variability. Figure 3.5 shows the its depths in different months and seasons together with the corresponding alongshore wind data, which is filtered using a 5^{th} order Butterworth low-pass filter with a cutoff of 10 days. Generally, the intermediate layer grows deeper from 6 m depth in summer to 7.5 m depth in winter. The monthly change has a similar tendency with the seasonal signal, with an exception in August, when it goes up to 5 m depth, which is also the shallowest depth during the whole time period. This unusual event can be caused by wind, which, in addition to fresh water input, also has a significant influence on the position of the interface. Wind during the nine months mainly has a down-inlet direction, and decreases rapidly from July to August and reaches its minimum strength in August, corresponding to the depth change of the interface, from 7 m in July to 5 m in August (Figure 3.5). Wind energy increases gradually from September to February with peaks in the winter time, associated with the increasing depth of the interface. It might be expected that in winter, with ice cover present, wind mixing would be reduced, but in these years relatively little

ice was present, wind is an important factor that influences the position of the interface over the sill, and strong wind events can deepen the surface mixed layer and increase the depth of the interface.

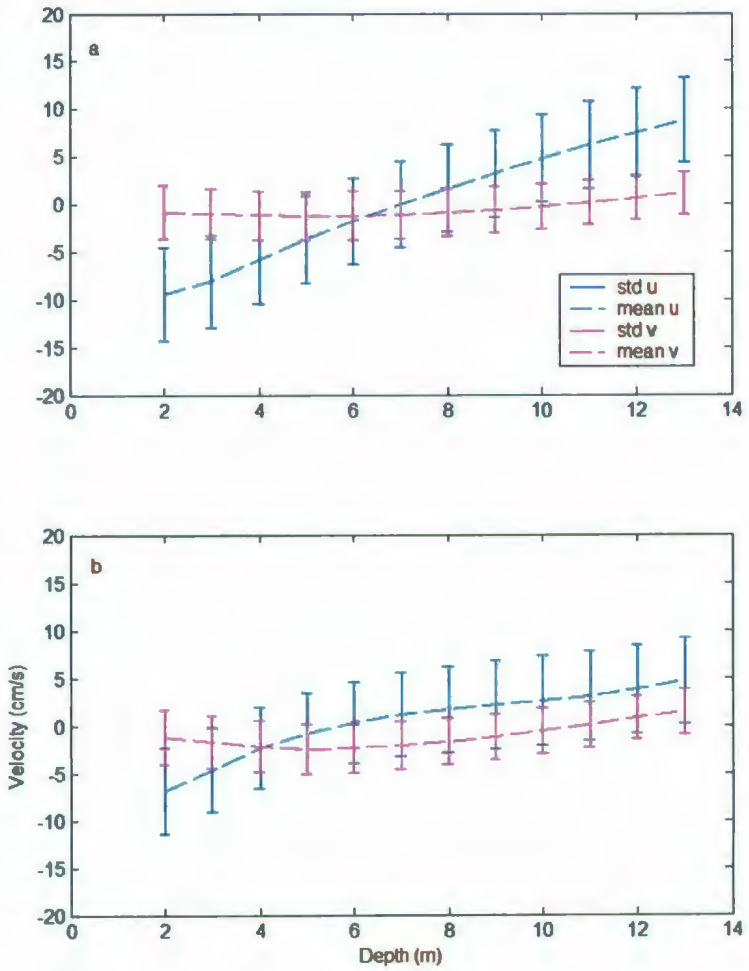

Figure 3.2: The mean alongshore velocity *u* and cross-shore velocity *v* at each depth, together with their standard deviations. a) The yearlong average velocity, b) summer average velocity. (+) denotes inflow, (-) denotes outflow.

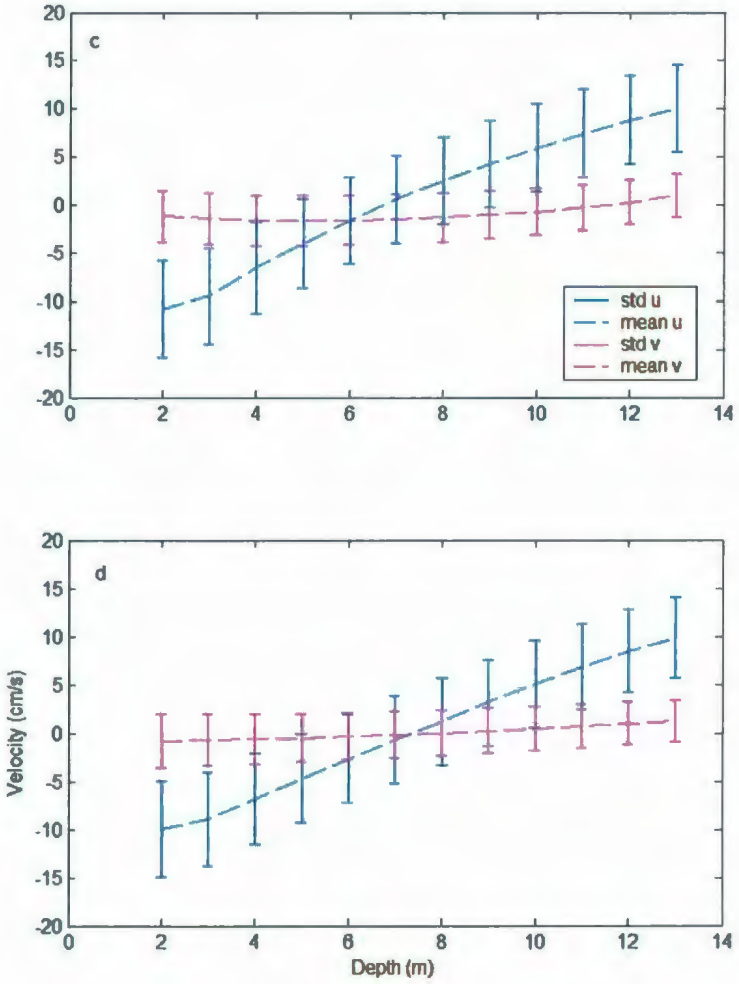

Figure 3.2 (continued): The mean alongshore velocity u and cross-shore velocity v at each depth, together with their standard deviations. c) Fall average velocity, b) winter average velocity. (+) denotes inflow, (-) denotes outflow.

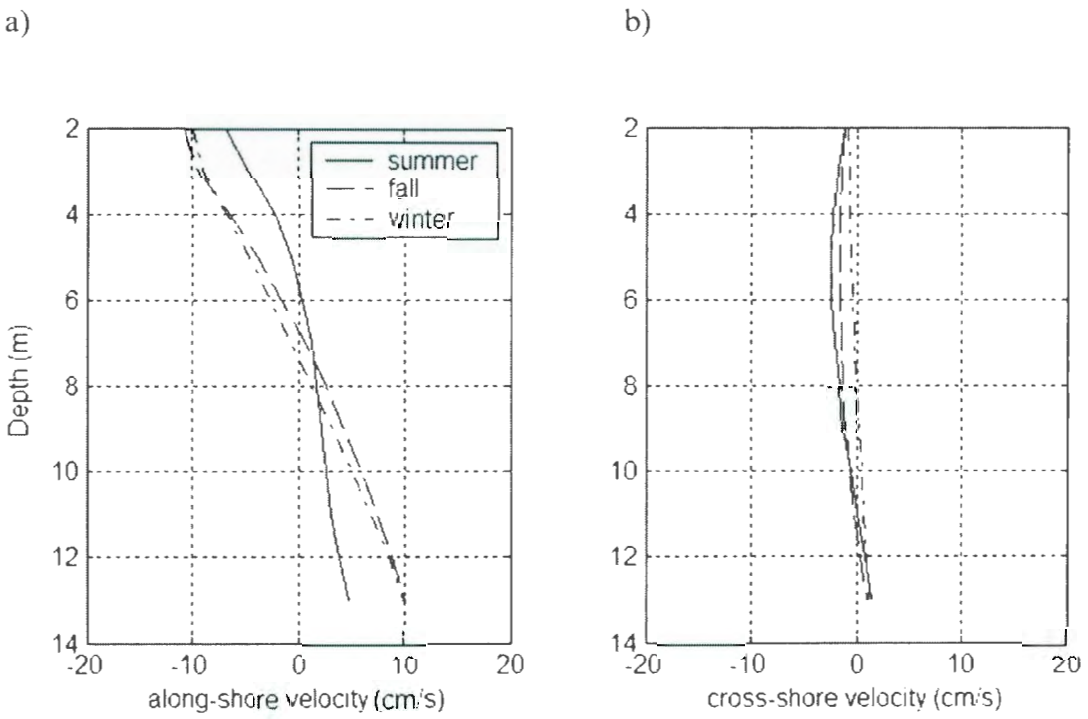

Figure 3.3: Seasonal average of, a) alongshore velocity u, and b) cross-shore velocity v, over the sill for summer, fall and winter, respectively. (+) denotes inflow, (-) denotes outflow.

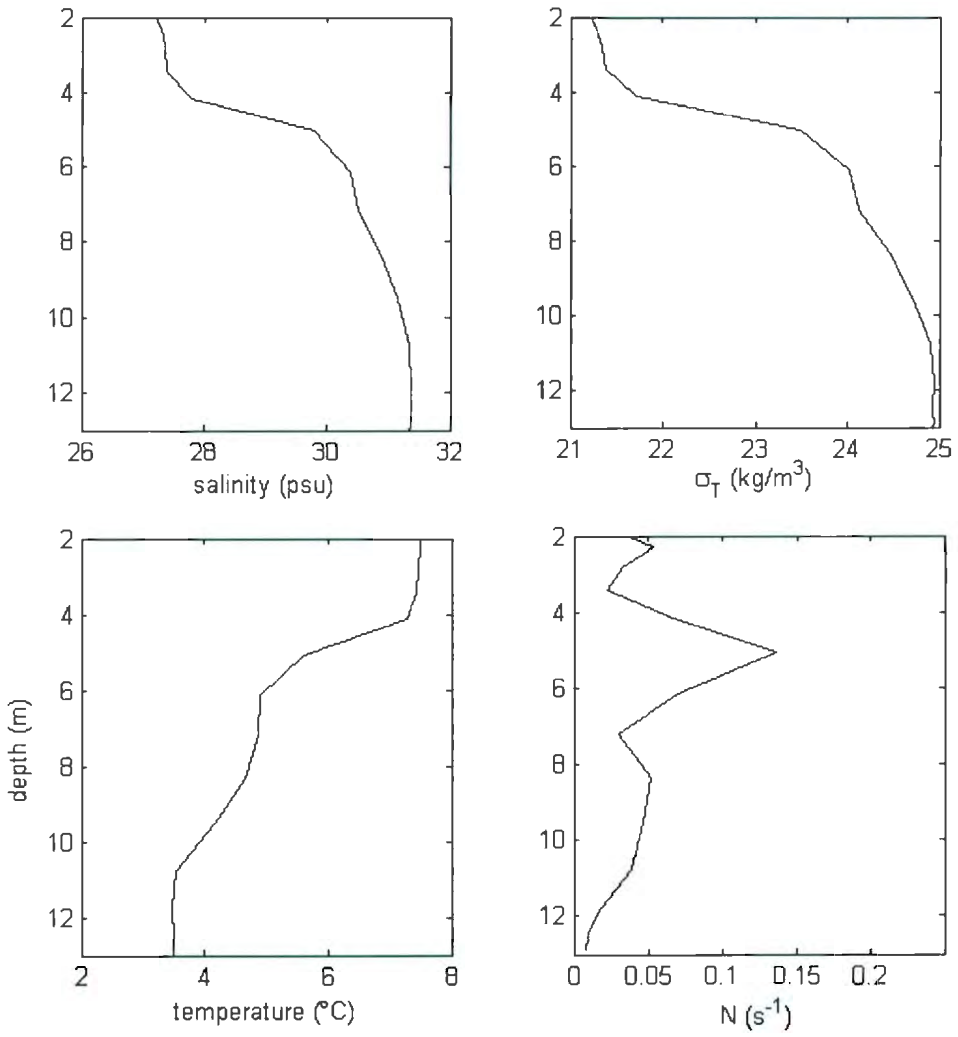

Figure 3.4: Vertical profiles of salinity, σ_T, temperature, and buoyancy frequency (see Section 5.2.1) over the sill from the CTD data sampled on June 14, 2006.

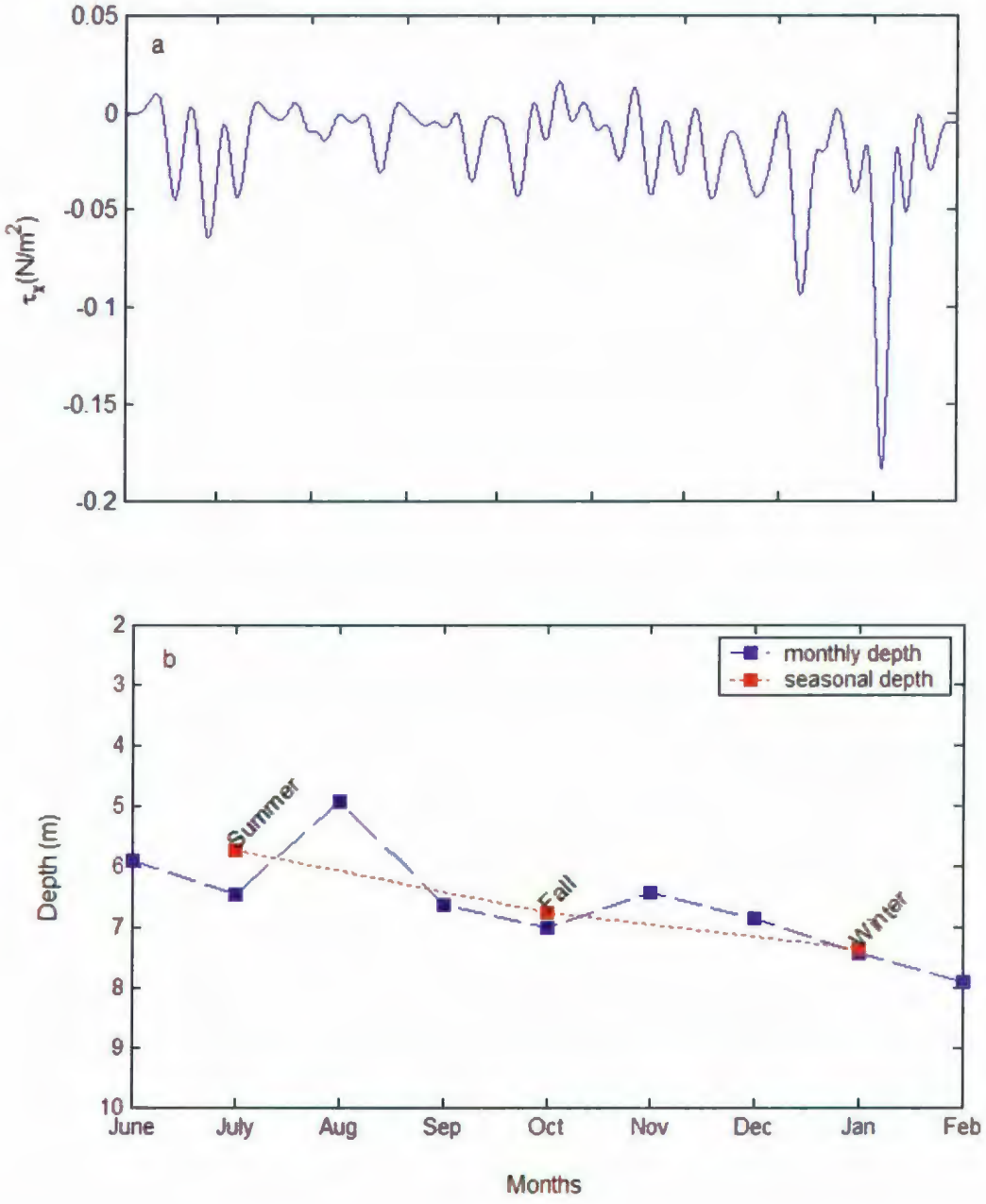

Figure 3.5: Time series of, a) alongshore wind stress from Norris Point weather station, and b) depths of *level of no motion* in each month and three seasons, from June 2006 to February 2007.

The influence of varying tidal forcing on the water properties through the water column are observable from 5-day time series (Figure 3.6). Tides with frequency of 2 cpd (semidiurnal oscillations) dominate the dynamics over the sill (Figure 3.6a). In addition to the velocity variation, plots of temperature, density and chlorophyll at the bottom all clearly show a response to the changing tide and display the semidiurnal cycles (Figure 3.6b-d). Both the bottom temperature and chlorophyll concentration increase with the inflow from the outer basin, and decrease with the outflow from the inner basin of the East Arm, whereas the bottom density decreases with the inflow and increases with outflow. The results illustrate the colder and denser outflow from the inner basin compared to the inflow from the outer basin, which is reasonable because the outflow is from the deep water in the fjord, which can be colder and also denser than the inflow from the surface area of the outer basin.

To support the results above, the vertical profiles of CTD data on both sides of the sill over several tidal cycles from June 9, 2004 to June 11, 2004, conducted by several cruises, are also used for this research. Sill-1 is within the inner basin of East Arm, and Sill-2 in the outer basin connected with the outer area. The BBO locates between the two sampling sites (Figure 3.7). The timeseries contours of temperature and density from each station are plotted relative to the tidal state (Figure 3.8 and 3.9, taken from Richards' thesis, 2005). It is clearly shown that the water in the inner basin (at Sill-1) is colder and denser than that in the outer basin (at Sill-2) at the same depth, which indicates the outflows from Sill-1 have lower temperature and higher density than the inflows from Sill-2. Additionally the time series plots of temperature and density data at Sill-2 are

without obvious regularities with the changing tide, probably due to unique location of Sill-2 where the circulation is more complicated owing to the influence by flows from the inner basin, South Arm and Gulf of St. Lawrence at the same time. The exchange process at Sill-1, on the other hand, shows a noticeable response to the tidal oscillations. During the out-flowing tide at Sill-1, for example, from 23 to 28 hours, both the isotherms and the isopycnals locate higher positions through the water column than the corresponding lines during the in-flowing tides from 30 to 35 hours, which also means that the outflow is colder and denser than the inflow (Figure 3.8). The similar situations can also be found at Sill-2 (Figure 3.9). Both the observations from 2004 and 2006 display the same results on the water properties from the inner fjord and the outer basin.

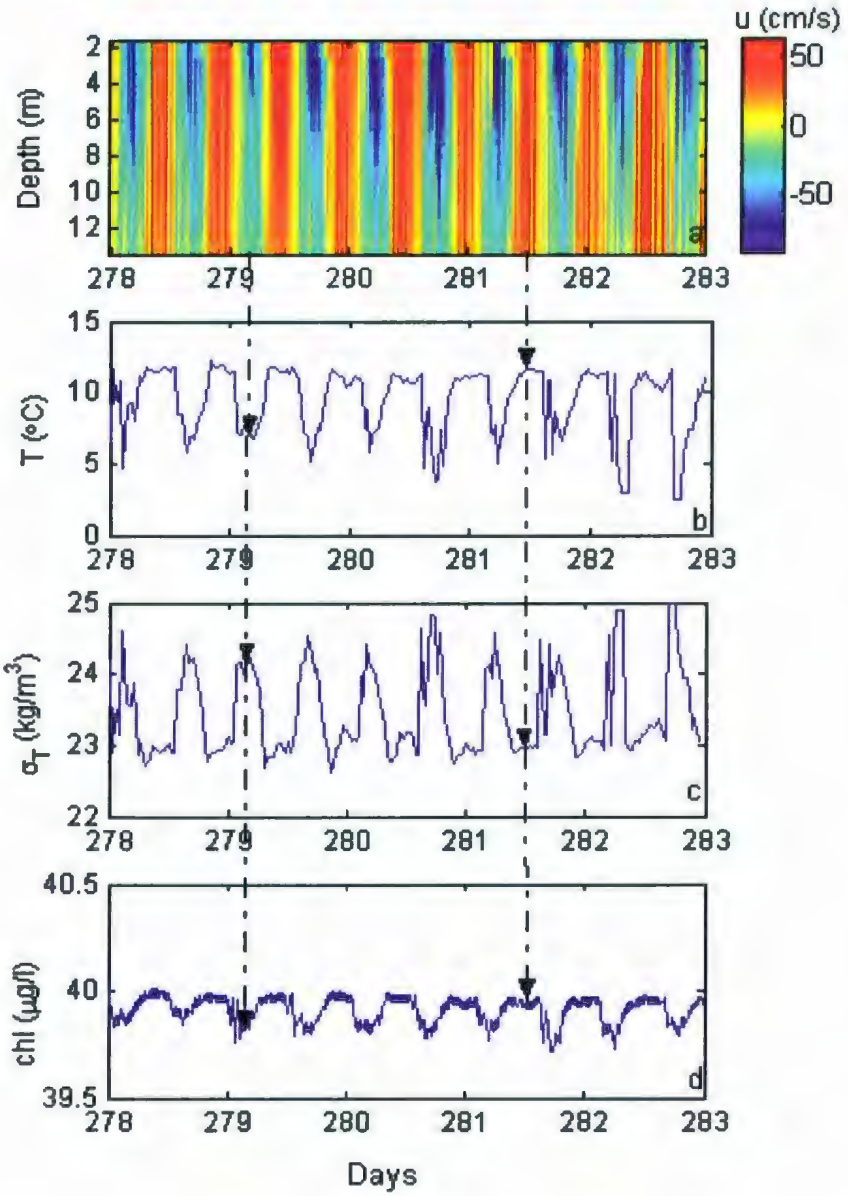

Figure 3.6: Time series of, a) alongshore velocity with (+) denoting inflow and (-) denoting outflow, b) bottom temperature c) bottom density, and d) bottom chlorophyll, from days 278 to 282.

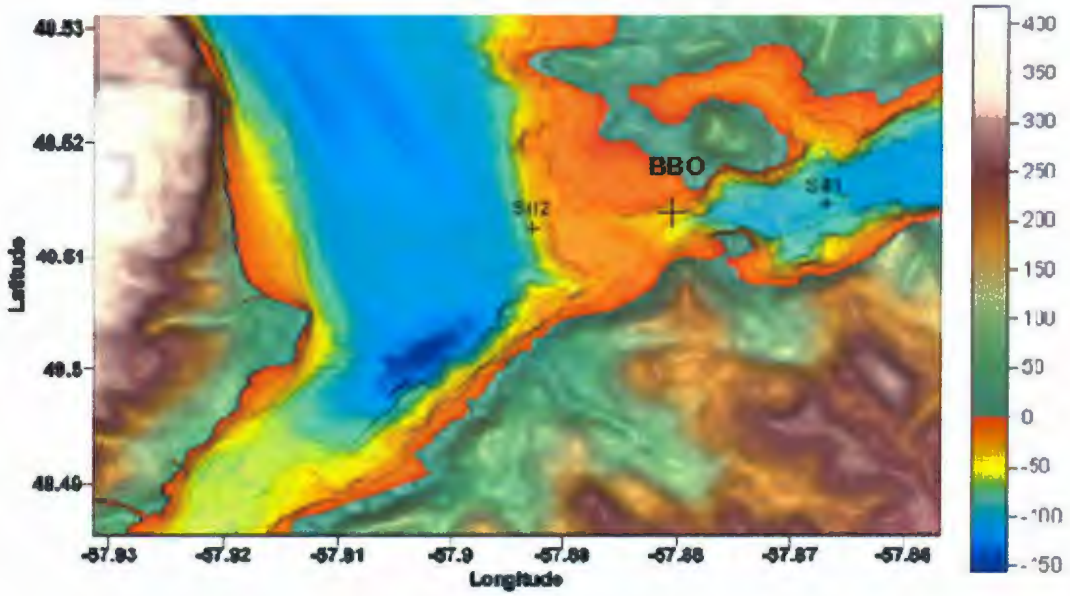

Figure 3.7: Sampling locations on either side of the sill, donated by Sill-1 and Sill-2, from June 9, 2004 to June 11, 2004, with location for BBO between them. Sill-1 is inside of the bay and Sill-2 is within the outer basin.

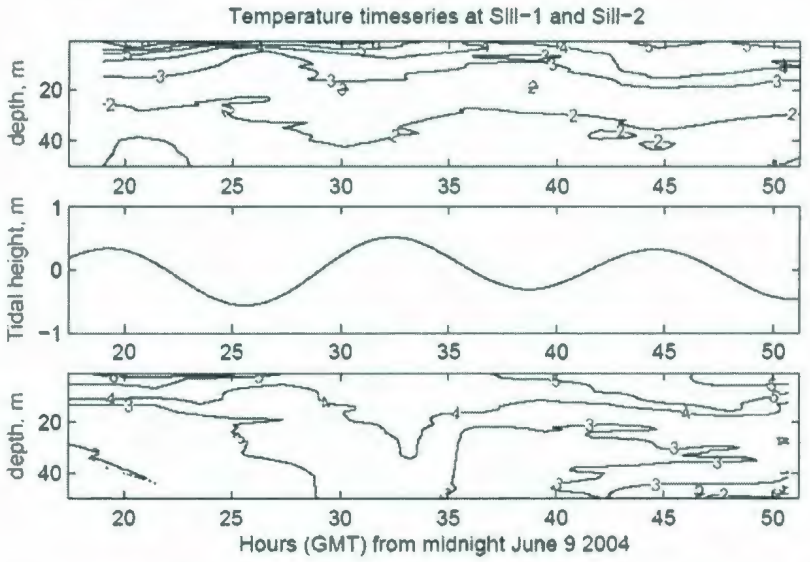

Figure 3.8: Time series of temperature sampled at Sill-1 (top) and Sill-2 (bottom) on June 9, 2004. The middle plot is the tidal state (Richards, 2005).

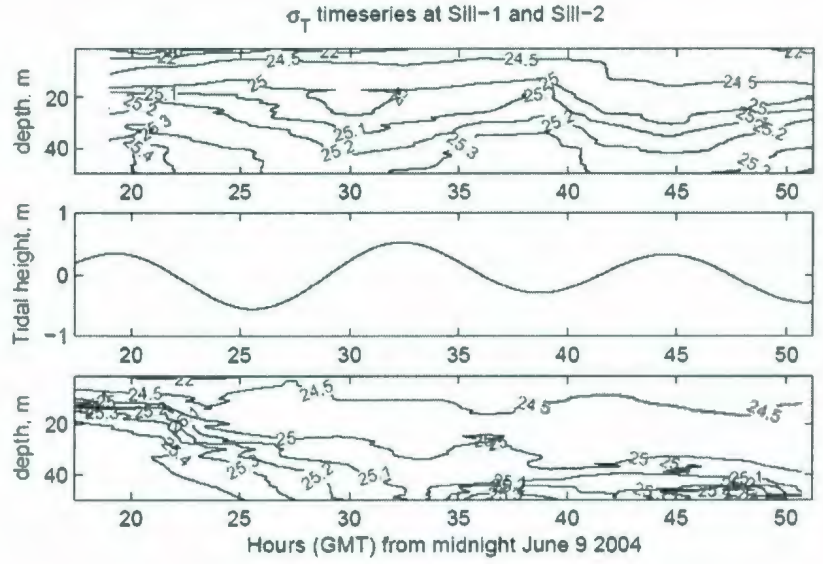

Figure 3.9: Time series of density sampled at Sill-1 (top) and Sill-2 (bottom) on June 9, 2004. The middle plot is the tidal state (Richards, 2005).

4 Tidal Currents

Tide is one of the dominant factors that influence the fjord circulation associated with vertical mixing, horizontal exchange and other small scale processes such as high frequency internal waves. Tidal currents over a sill are strongly amplified due to its shallowness and are thus of great important. The preliminary analysis (Figure 3.6) shows that the semidiurnal tides are the dominant components through the water column and the analysis following will present the tidal structures over the sill as well as the details on selected tidal constituents.

4.1 T_Tide Analysis

The harmonic tidal analysis developed by M. Foreman (1977), is commonly used to predict tidal currents. The principle of the analysis is to assume that the ocean tides can be decomposed into a series of tidal constituents with the form of a combination of sine and cosine functions, and each constituent has a specified frequency and initial phase. The T_TIDE analysis based on Foreman tidal analysis has the advantage over other methods to use complex algebra for vector time series instead of dealing with each component separately (Pawlowicz et al. 2002), and is applied to the time series of ADCP data at each depth for this research.

The alongshore velocity amplitudes of selected tidal constituents at the surface are shown in Figure 4.1. The M_2 tide is the most significant component which contributes a 70% of the total tidal kinetic energy and has a four times larger amplitude than the next largest constituent S_2. This result agrees with what Richards (2005) found in his thesis

using ADCP data in 2003 from the same area. The shapes of the major tidal constituent velocities at all depths, however, have no uniform pattern (Figure 4.2): the semidiurnal M_2 tide is depth dependent and has a distinct mode-1 baroclinic structure in the vertical direction; the other three constituents, probably due to their weak signals compared to M_2, on the other hand, show little depth dependence in the amplitudes and have no remarkable structures through the water column. This is contrary to the result from Richards' thesis that the velocities of all major constituents decrease with depth over the sill (Richards, 2005). The parameters of tidal ellipses at each depth are calculated by T_TIDE analysis and the details of the major tidal constituents are summarized in Table 4.1. Both the axes of the representative tidal ellipses and the corresponding Greenwich phase can give a detailed description about each tidal constituent. The inclination of the ellipse indicates the angle the semi-major axis makes with the positive x-axis (east direction). A positive value for the length of the semi-minor axis indicates that the current rotates counter-clockwise around the tidal ellipse, while a negative value indicates a clockwise rotation.

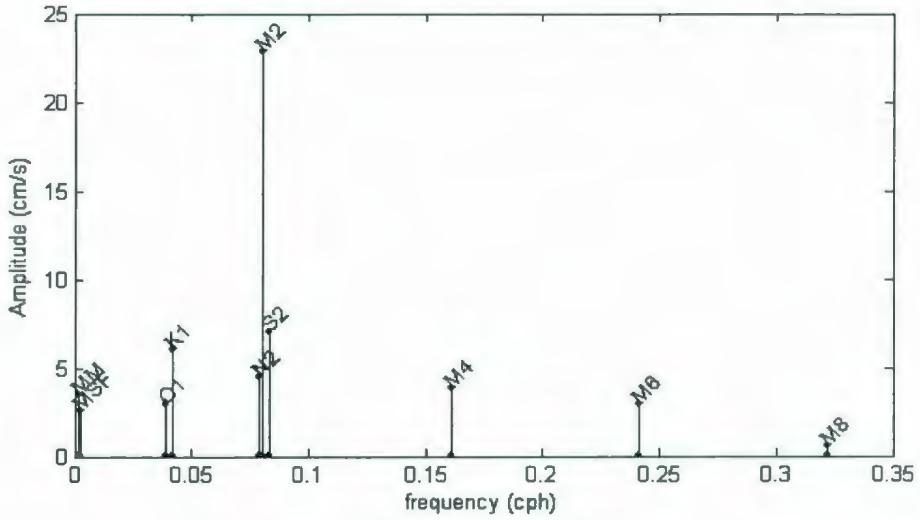

Figure 4.1: Alongshore velocity amplitudes of significant tidal constituents at the surface, calculated from T_TIDE scripts using BB06_b ADCP data, from June 21 to September 11, 2006.

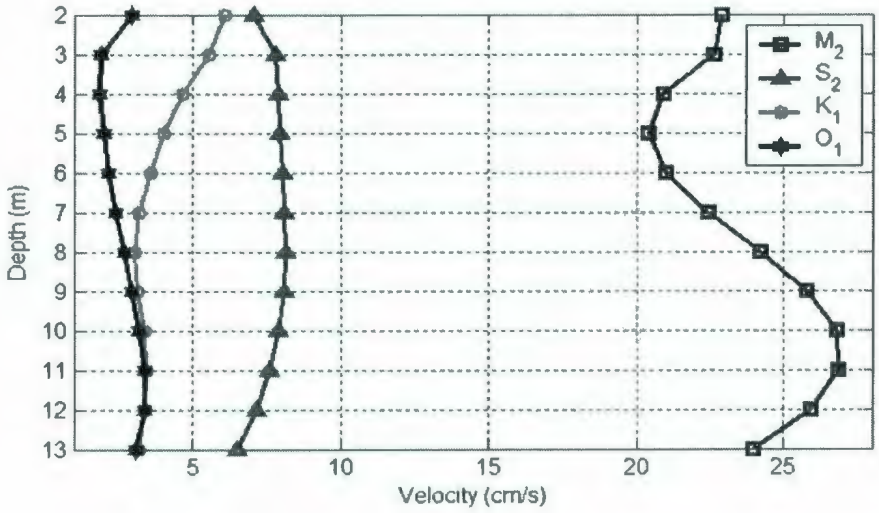

Figure 4.2: Alongshore-velocity amplitudes of selected tidal constituents at all depths, between June 21 and September 11, 2006, from T_TIDE analysis.

M_2 and K_1 as the most energetic constituents at the semidiurnal and diurnal bands, respectively, are selected to be the representative tidal constituents at each frequency, which will be further analyzed to investigate the characteristics of dominant tidal currents over the sill. Figure 4.3 contains the phase plots of M_2 and K_1 constituents, respectively. The phases of K_1 tide do not have significant changes at different depths, roughly 20 to 50 degrees; whereas the phase of M_2 tide vary about 180°at 7 m depth indicating a strong baroclinic response primarily in mode 1 at that position (Figure 4.3). The three-dimensional M_2 and K_1 tidal ellipses through the water column are shown in Figure 4.4 and 4.5, respectively, and the blue line connects the inclination of each ellipse at different depths. K_1 signals show roughly consistent inclination and magnitude with depth, and are weak over the sill giving the amplitude ratio K_1/M_2 about 1/7. The M_2 tidal ellipses show approximately constant strength with increasing depth, while the inclinations vary from several degrees to 180° at 6 m depth, which means that the deeper currents below 6 m depth are towards the opposite direction to the flows above this depth. The amplitude and phase distributions of K_1 and M_2 constituents indicate that K_1 constituent is more nearly barotropic than the M_2 tide over the sill.

Table 4.1: Harmonic constants of main tidal constituents, calculated by T_TIDE analysis.

Depth (m)	Name	Frequency (cph)	Major Axis (cm/s)	Minor Axis (cm/s)	Inclination (°)	Greenwich Phase (°)
3	MM	0.0015122	2.4136	0.73957	172.36	269.95
	O_1	0.038731	1.8701	0.34334	3.3382	149.03
	K_1	0.041781	4.6559	-0.27217	175.74	29.548
	M_2	0.080511	20.906	2.9914	3.5182	333.53
	S_2	0.083333	7.9161	0.58505	7.0377	10.601
5	MM	0.0015122	1.6611	0.70172	143.15	230.11
	O_1	0.038731	2.1641	0.050252	5.5874	147.99
	K_1	0.041781	3.5592	-0.25841	177.79	12.837
	M_2	0.080511	21.023	3.0848	179.89	148.33
	S_2	0.083333	8.0465	0.44222	4.6172	7.4387
7	MM	0.0015122	1.3496	-0.50389	125.33	180.54
	O_1	0.038731	2.6769	-0.30736	0.44655	151.48
	K_1	0.041781	3.0435	0.18037	179.16	348.76
	M_2	0.080511	24.182	2.8099	176.99	146.83
	S_2	0.083333	8.1446	0.23469	179.65	186.4
9	MM	0.0015122	2.256	-0.73724	176.7	111.3
	O_1	0.038731	3.1851	-0.41025	174.39	335.2
	K_1	0.041781	3.3695	0.40438	174.71	325.99
	M_2	0.080511	26.793	2.2593	175.83	147.4
	S_2	0.083333	7.9194	0.23201	174.47	188.31
11	MM	0.0015122	3.6819	-0.066616	172.72	99.252
	O_1	0.038731	3.3565	-0.44277	172.83	337.48
	K_1	0.041781	3.405	0.61074	171.82	314.03
	M_2	0.080511	25.924	1.2068	175.61	146.97
	S_2	0.083333	7.168	0.10312	172.11	189.13

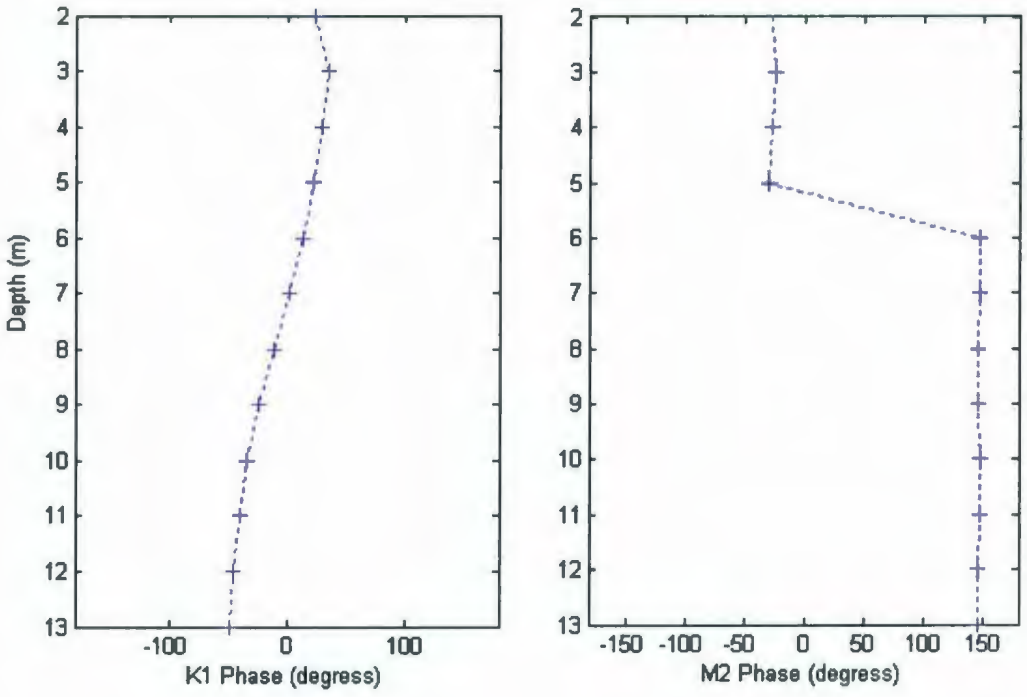

Figure 4.3: Phase plots of K_1 and M_2 tides, respectively, at each depth using the BB06_b ADCP data, from June 21 to September 11, 2006.

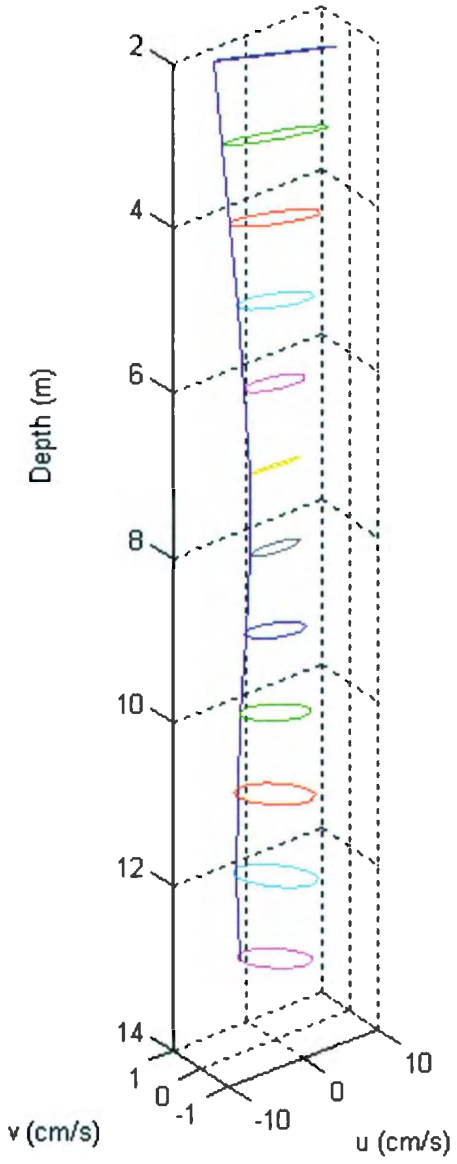

Figure 4.4: The K_1 tidal ellipses at each depth, using ADCP data from June 21 to September 11, 2006. The blue line connects the inclination of each ellipse.

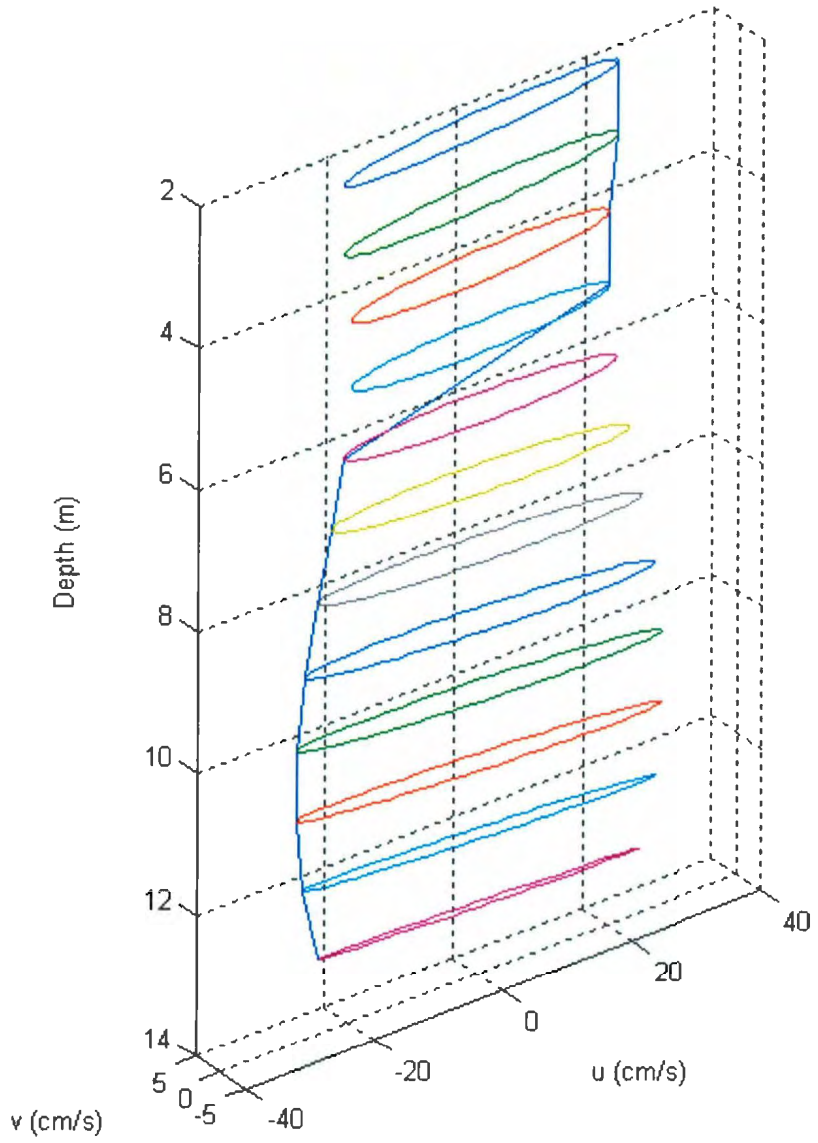

Figure 4.5: The M_2 tidal ellipses at each depth, using ADCP data from June 21 to September 11, 2006. The blue line connects the inclination of each ellipse.

4.2 Barotropic and Baroclinic Tides

4.2.1 Theory

There are two general features of tidal motion in a stratified ocean: the barotropic surface wave with horizontal velocities independent of depth, and baroclinic internal waves, the horizontal currents of which have the vertical oscillations (Ray et al. 1996). Driven by the gravitational forcing from the sun and moon, the surface, or barotropic tide is fairly regular and is associated with sea level changes at tidal frequencies. The baroclinic tide is an internal wave at the tidal frequency generated when barotropic tide interacts with various topography features in a highly stratified ocean, such as continental shelf or sill. It is associated with vertical displacements of isopycnals and considered to be the major process that extracts energy from barotropic flow. When the barotropic tide passes through a fjord, energy is lost by generating internal tides, bottom friction and high-frequency internal waves (deYoung and Pond, 1989). The dissipation of internal tides results in the production of internal waves which then generate turbulence. Internal tides can be observed by instruments that sample within the water column but they may be inconclusive and sometimes contradictory (Chiswell et al. 1998).

Previous research has indicated that internal tides can be generated on both sides of the sill in a fjord (Webb and Pond, 1986; deYoung and Pond, 1987), and over the sloping shore near the head of the fjord (Farmer and Osborn, 1976). Here I will briefly review some basic theory on internal tides. A comprehensive review of internal tide theory and observation is given by Wunsch (1975): in spherical coordinate system, θ is latitude, λ is longitude measured eastward, N is buoyancy frequency, u, v are horizontal

velocities, w is vertical velocity, p is the perturbation pressure, and f is the Coriolis parameter,

$$\begin{aligned} u &= U(\theta,\lambda)F_z(z) \\ v &= V(\theta,\lambda)F_z(z) \\ w &= W(\theta,\lambda)F(z) \\ p &= P(\theta,\lambda)F_z(z) \end{aligned} \tag{4.1}$$

then the Laplace tidal equations based on Boussinesq and linear wave approximations are

$$\begin{aligned} &-i\omega U - fV = -(1/a)\frac{\partial P}{\partial \theta} \\ &-i\omega V + fU = -(1/a\sin\theta)\frac{\partial P}{\partial \lambda} \\ &\frac{1}{a\sin\theta}\frac{\partial}{\partial\theta}(U\sin\theta) + \frac{1}{a\sin\theta}\frac{\partial V}{\partial\lambda} - \alpha_n^2 i\omega P(\theta,\lambda) = 0 \\ &\left[\omega^2 - N^2(z)\right]\frac{F(z)}{F_z(z)} = \frac{-i\omega P(x,y)}{W(\theta,\lambda)} \end{aligned} \tag{4.2}$$

where ω is the frequency of a single tidal constituent, f is the Coriolis parameter, and α_n are a set of eigenvalues determined from

$$F_{zz}(z) + \alpha_n^2(N^2(z) - \omega^2)F(z) = 0\,. \tag{4.3}$$

With given boundary conditions and for the water that has constant depth D and a slowly varying $N(z)$, equations (4.2) and (4.3) yields the lowest mode eigenvalues,

$$F = A_0 \sin N(z+D)/(gD)^{1/2} \cong A_0 N(z+D)/(gD)^{1/2} \tag{4.4}$$

which is linear in the vertical velocity, and the higher-order mode with n-nodes in the vertical is

$$F(z) = A_n \sin n\pi(z+D)/D \tag{4.5}$$

where n is integer. The solutions to the governing equations thus can be divided into two parts, a surface wave with constant horizontal velocities, linear vertical velocity with depth, and maximum vertical displacement at surface; and internal waves with oscillatory horizontal and vertical velocities with depth and maximum vertical displacement within the water column. Those are barotropic and baroclinic motions, respectively. When a beta plane approximation $f = f_0 + \beta y$ is applied to the Laplace equations, solutions on an unbounded mid-latitude beta plane with constant f can be written as

$$V = Ae^{ikx}$$
$$k = -\frac{\beta}{2\omega} \pm \frac{1}{2}\left[\frac{\beta^2}{\omega^2} + \frac{4(\omega^2 - f^2)}{gh_n}\right]^{1/2} \tag{4.6}$$

Freely traveling waves are only permitted when k is real, which can not be fulfilled at the 'critical' or 'inertial' latitude, where $\omega \cong f$. For location conditions, beta terms are negligible and f is constant, the equations reduce to

$$\nabla^2 V + [(\omega^2 - f^2)/gh_n]V = 0 \qquad f = const \tag{4.7}$$

Clearly freely traveling waves are possible only when $\omega^2 > f^2$. The critical latitudes are 30° for diurnal motions, 60° for semidiurnals. If the forcing (tidal) frequency is superinertial, and also below the buoyancy frequency N, the internal oscillations may propagate away from the generation site as plane internal waves. The angle that wave characteristics (group velocity) makes with the horizontal φ:

$$\tan^2 \varphi = \frac{\omega^2 - f^2}{N^2(z) - \omega^2} \tag{4.8}$$

Previous results from T_TIDE analysis show that K_1 and M_2 tidal constituents make significant contributions to the tidal forcing at the diurnal and semidiurnal bands,

respectively. The latitude of Bonne Bay however gives $f_0 = 2\Omega \sin\theta$ =1.5cpd; internal tides therefore can theoretically exist at semidiurnal bands, not at diurnal bands. Observations of amplitude and phase features of M_2 and K_1 in Section 4.1 also indicate the same results. The following analysis will focus on M_2 internal tide to examine its vertical structure through the water column together with the temporal variability of both M_2 barotropic and baroclinic motions above a single location over the sill.

4.2.2 Observation and Analysis

M_2 phase and amplitude contour plots (Figure 4.6) show that there is 180° phase shift in u between upper and lower layers at 6 or 7 m depth, from June to August when M_2 amplitudes intensify at the bottom, which indicates a strong baroclinic response; phase keeps uniform with depth in fall and winter, and amplitudes during the same time have a clear surface intensification, representing the barotropic motions. As expected, given the change in stratification from summer to winter with the increasing depth of the surface mixed layer and the reduced stratification between the upper and lower layers, there is only M_2 baroclinic response over the sill in summer, with no evidence of baroclinic signals after summer.

To separate baroclinic currents from the barotropic in summer, time series of depth-averaged horizontal velocities $\frac{1}{h_0}\sum_{i=1}^{z}(u_i, v_i)$ from ADCP is taken as the barotropic components since they are theoretically constant with depth. Baroclinic currents have zero depth integral and thus they are the residual currents obtained by removing the barotropic signals from the measured currents. All the time series are harmonically

analyzed to give the phase and amplitude information on each component. To reliably separate M_2 tide from their neighboring S_2 constituent in the harmonic analysis, the data record should be of sufficient duration,

$$|f_m - f_R|T > R \tag{4.9}$$

where T is the record length, R is usually equal to unity, f_m, f_R are the frequencies of two neighboring tidal constituents, respectively (Emery et al. 1998). For this research, separation of the next most significant semidiurnal constituent S_2 (0.0833 cph) from the principal component M_2 (0.0805 cph) requires a record length $T > 1/|f(M_2) - f(S_2)| = 14.7$ days.

Harmonic analysis is performed on 16-day segments of horizontal velocity data which permits the accurate separation of each constituent. Harmonic constants of depth-averaged currents (barotropic) and of deviations from theses averages (baroclinic) are plotted as tidal ellipses in Figure 4.7 and 4.8. The horizontal tidal velocity vectors of the barotropic flow have energetic alongshore component but weak cross-shore one (Figure 4.7). Their tidal ellipses are aligned preliminary in the alongshore (east-west) direction and rotate counterclockwise (with negative semi-minor axis values) in accordance with shelf-modified Kelvin wave dynamics (Munk et al. 1970). For unidirectional, freely-propagating internal waves, the major axis points in the direction of horizontal wave propagation; the orientations of barotropic tidal ellipses are down-inlet, consistent with the direction of the outflow at the surface. The velocity amplitudes of barotropic tides are almost constant during the whole time series, ~25 cm/s in semi-major axis. In contrast, Figure 4.8 shows that the corresponding baroclinic ellipses are less polarized and most of

them rotate clockwise (with positive semi-minor axis values), consistent with kinematics of freely propagating, unidirectional internal waves in the northern atmosphere (Lerczak et al. 2003). The M_2 baroclinic tide has the vertical structure expected for mode-1 internal waves, with the minimum amplitudes at mid-column, ~1 or 2 cm/s in semi-major axis, and maximum near the top and bottom, ~ 5 to 6 cm/s, much weaker than the barotropic tidal amplitudes.

The internal tide is an important sink for barotropic tide energy. Webb and Pond (1986) have calculated that internal tides contribute 40% of the total lost from barotropic tide in Knight Inlet, British Columbia. The ratio of baroclinic to barotropic tidal kinetic energy in Bonne Bay calculated grossly using the velocity amplitudes is around 20%. The result suggests that the semidiurnal internal tides contain one fifth of the surface tide energy. Additionally, friction over the sill, and high-frequency internal waves are other sinks for barotropic energy. Freeland and Farmer (1980) estimated that only about 3% of the energy lost from the barotropic tide goes into the friction with a short sill. Friction can however be significant when a fjord has a shallow (15-20 m) sill, which could be 50% of the total loss (deYoung and Pond, 1989). Very little energy is transferred to high-frequency internal wave, around 5% suggested by Stacey and Zedel (1986). Based on previous literature, we suggest that friction and internal tide are the dominant energy sinks for the barotropic tide at the Bonne Bay sill. Energy from internal tide will be transferred to other nonlinear motions dissipated or to contribute mixing. The orientation in the alongshore plane of group velocity of the M_2 internal tide is nearly 0° determined by equation (4.8), which indicates that the energy in the internal tide is concentrated in a

beam parallel to the horizontal. The propagation speed of the lowest-mode internal waves is expected to be $C = Nh/\pi$ where N is the buoyancy frequency, h is the water depth. Then the wavelength λ of M_2 internal tide can be analytically determined as $\lambda = CT$, where T is the wave period. In Bonne Bay, the period of M_2 baroclinic tide, $T = 12.42$ hours, and the depth-averaged buoyancy frequency $N = 0.043$ s^{-1} result in $C = 16$ cm/s, $\lambda = 7$ km.

According to the harmonic constants (amplitude, phase) calculated by T_TIDE analysis, the baroclinic currents do not bear a constant phase relation to the surface tide that generates it, which means that there is also no coherence between barotropic and baroclinic motions and thus the M_2 internal tide is not generated locally but is propagating into the region from the generation place (Holloway, 1984). The horizontal velocities have also been separated every 7 days to investigate spring-neap tidal cycles. Results indicate that the barotropic tide has a pronounced spring-neap pattern, whereas the semidiurnal internal tide time series do not show this cycle.

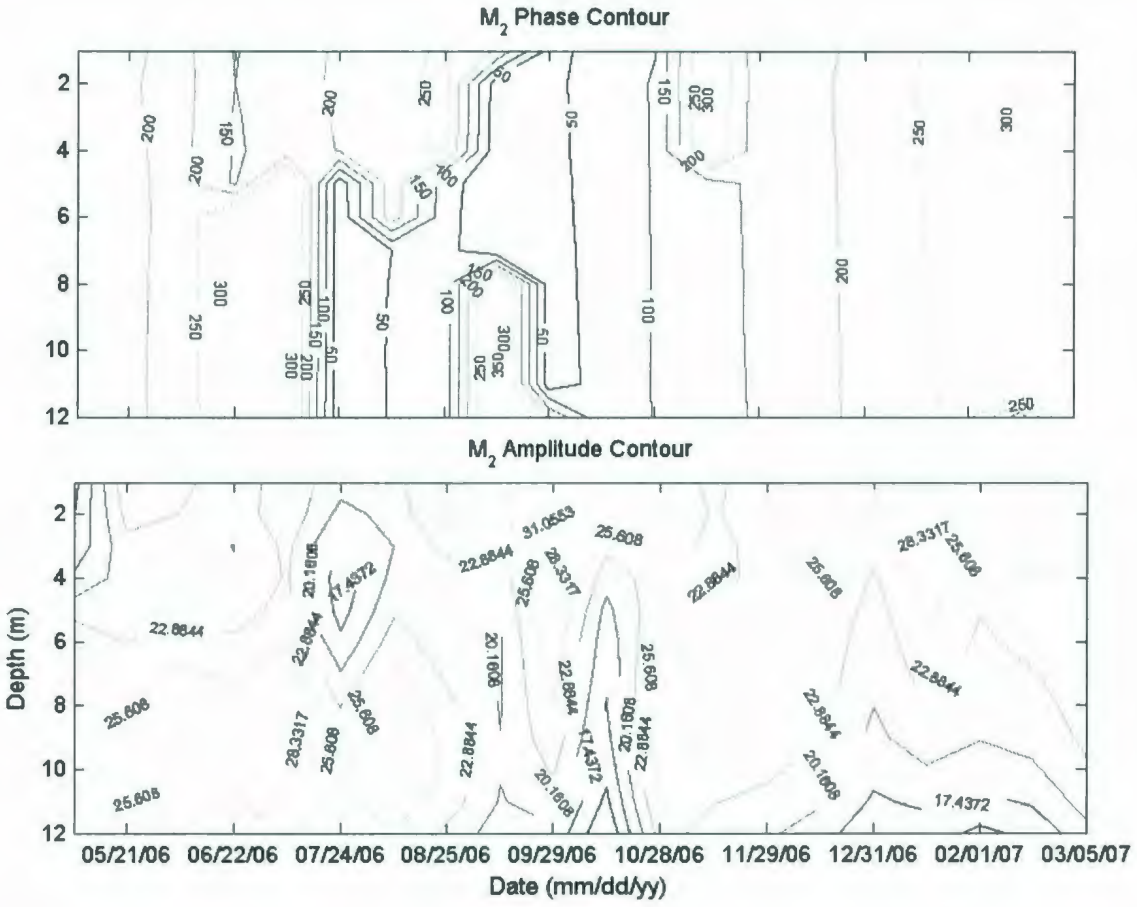

Figure 4.6: Contour plots of M_2 phase and amplitude through the yearlong time between May 2006 and March 2007. Harmonic constants are calculated by T_TIDE analysis.

For the diurnal band K_1, the internal tide cannot be observed or measured over the sill even in summer when the water has the strongest stratification (Figure 4.3). Wunsch (1975) indicated that theoretically free diurnal internal tides may not be generated to the north of the diurnal inertial latitude. Besides the diurnal barotropic tides are much weaker than the semidiurnal in Bonne Bay, and hence the driving force is not strong enough to generate internal motions. Energy of internal tides is carried out by resonant interactions,

internal waves, and friction through viscous force, internal tides could also be absorbed by critical layers when they are breaking in the main thermocline.

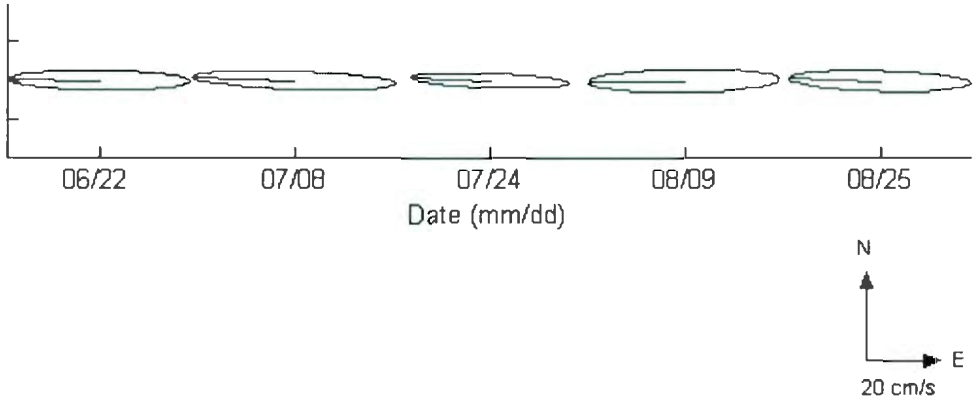

Figure 4.7: Time series of M_2 barotropic tidal ellipses obtained from the depth-averaged current between June 22 and August 25, 2006. The line from the ellipse center shows the maximum velocity, and the orientation of the ellipse is relative to the horizontal plane with alongshore (E) and cross-shore (N) axes.

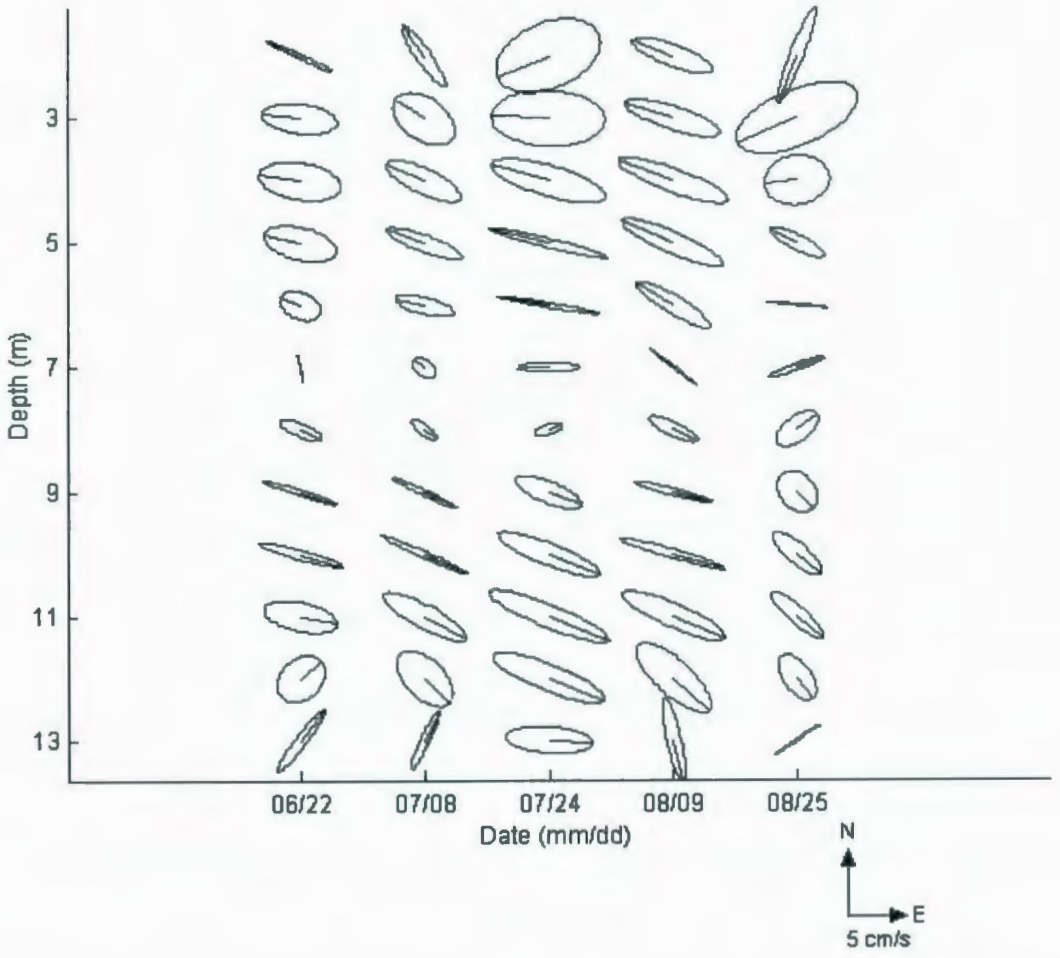

Figure 4.8: Time series of computed M_2 baroclinic tidal ellipses obtained by removing the barotropic component from the measured current between June 22 and August 25, 2006. The line from the ellipse center shows the maximum velocity, and the orientation of the ellipse is relative to the horizontal plane with alongshore (E) and cross-shore (N) axes.

5 Subtidal and High-Frequency Flows

The analysis in previous chapter presents motions at tidal frequencies. Non-tidal currents in addition to tides are also observed over the sill, including subtidal flow with a significant amount of kinetic energy at frequencies less than one cycle per day, and high frequency internal waves with period around an hour. In this chapter, the analysis will focus on the flows at several different timescales, from days to months for subtidal flow, and several hours for high-frequency internal waves, respectively.

5.1 Subtidal Currents

Subtidal flows have been often observed in fjords or estuaries, and factors associated with this low-frequency flow in an ocean channel include wind forcing, current outside the mouth of the channel, shelf processes, and horizontal stratification attributed to the changes in freshwater discharge (Farmer and Freeland, 1983). The subtidal exchange process with period from days to months is associated with the deep water renewal of the fjord (deYoung and Pond, 1988). The effects of external forcing on renewal events have been extensively explored, while little consideration of internal forcing has been received (Geyer et al. 1982).

5.1.1 Observations

The Power Spectral Density technique is performed to the time series of alongshore velocity data. As the data set can be considered as a random time series, spectral analysis is a useful tool to interpret them and investigate the kinetic energy

distribution. A modified periodogram method, named the Welch method, is applied in this research. According to the power spectral density plot of alongshore velocity at all depths (Figure 5.1), it is clear that tides dominate the energy spectrum, including semidiurnal and diurnal tides together with constituents at the frequencies of 4 and 6 cycles per day. And also, there is strong energy distribution at the frequency below 1 cycle per day; the peak is obviously not tidally forced and it is thought to be the subtidal component. Energy at this period shows substantial depth dependence with a minimum centered at 6 m, and maximum at the surface and below 8 m. The observation reveals strong low-frequency inflow that extends from 8 m depth to the bottom, and the energetic surface outflow is restricted to the upper 4 m. The power spectrum is however fairly uniform with depth at higher frequencies, and no energetic motions with frequencies above 8 cpd can be observed from this alongshore velocity power spectrum.

5.1.2 Wind Forcing

In order to examine the effects of wind forcing on the low-frequency subtidal flows over the sill, the wind data and alongshore velocity are low-pass filtered using a fifth order Butterworth filter with the cutoff frequency of 30 hours to remove the energy from all the tidal signals and high frequency components. The residual is then considered to be the subtidal current. Richards (2005) found that the subtidal flows in Bonne Bay fjord are highly correlated with the alongshore wind stress; the squared coherence between surface wind and alongshore velocity is over 0.6 for frequencies between 0.2 and 0.5 cpd from data sampled in 2002 and 2003. The velocity and wind data from 2006 however are weakly coherent with squared coherence below 0.2 at any frequencies,

which suggests that local wind forcing is not a significant factor that influence the subtidal flow during the year 2006.

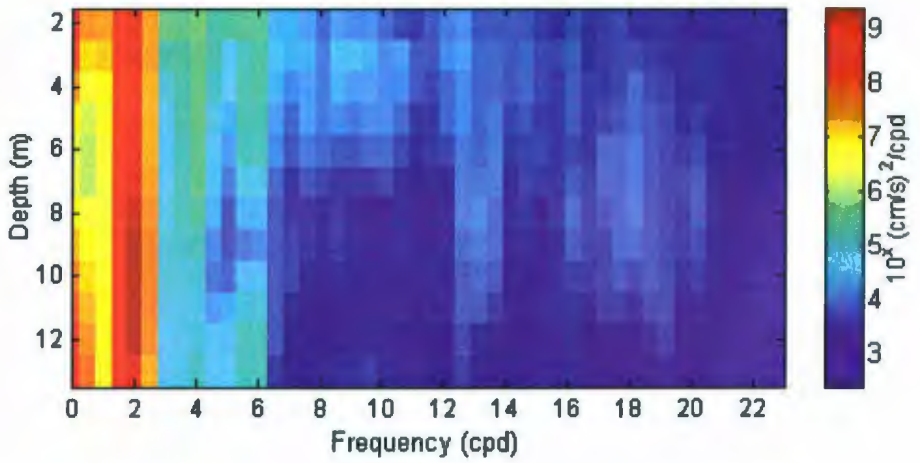

Figure 5.1: Power Spectral Density (PSD) of alongshore velocity at all depths using the BB06_b ADCP data, from June 21 to September 11, 2006. The sampling rate is 30 minutes and the number of degrees of freedom is 21.

5.1.3 Internal Forcing

In addition to wind forcing, gravitational circulation driven by baroclinic pressure gradients is another primary influence on the low-frequency currents and horizontal transport in an estuary system (Ribeiro et al. 2004). Due to the input from both freshwater and seawater, the horizontal density gradient is a typical characteristic of many estuaries. Driven by this gradient, gravitational circulation is characterised by a seaward current at the surface and a landward flow at the bottom. Tide is an important forcing that

influences mixing, and thus the variations of tidal amplitudes due to the spring-neap tidal cycles can modulate the horizontal stratification. There are theoretical and observational studies before suggesting that the low-frequency exchange process in an estuary could respond to the modulation of stratification driven by spring-neap tidal cycles (Monismith et al. 1996; Geyer et al. 1982), with maximum stratification occurring during neap tides when tidally generated mixing is at a minimum, and minimum stratification during spring tides when maximum mixing occurs.

To look at how tide amplitudes can influence on the long-term non-tidal flow in Bonne Bay fjord, the long-term variability is investigated using a 70-day time series of alongshore velocity data from ADCP between late September and November 2006, a period when the fjord has uniform river discharge. Harmonic analysis is applied to horizontal velocity vectors to obtain the time series of tide amplitudes at the surface. Bottom velocity and wind vectors in the alongshore direction are low-pass filtered with a cutoff frequency of 30 hours. The 70 days of the study comprise five spring-neap cycles (Figure 5.2b), including two stronger springs, on days 282 and 312, and three weaker ones, on days 265, 298 and 328. The low-pass filtered bottom velocity illustrates the behaviour of the subtidal flow over these five consecutive spring-neap cycles. The increased subtidal flow, with inward velocities exceeding 35 cm/s at the bottom, occurs during neap tides with peak on day 262, 287 and 303. No clear signal of similarly intensified deep-water renewal is present during the fifth neap tide between days 315 and 322. Subtidal flows show a very limited or insignificant response during spring cycles, with inward velocity amplitude below 10 cm/s except a stronger event during the third

spring cycle between days 293 and 298 with bottom velocity amplitude over 20 cm/s. The results suggest that spring-neap tidal cycles appear to be highly correlated with low-frequency event over the sill, which is associated with the deep-water exchange events.

The strong inward flow during the third spring tide is conjectured to be evidence of the additional effect of wind stress, since it is obvious that the strong inflow between days 293 and 298 during the third spring tide is coincident with the peak landward wind stress of up to 0.8 N/m^2 (Figure 5.2a). Richards (2005) found that in Bonne Bay the surface winds influence both the magnitude and direction of flow through the entire water column over the sill: the up-inlet wind causes a deceleration of the flow, while down-inlet wind results in an acceleration of the flow in both layers. The explanation of the unusual event between days 293 and 298 in 2006 could be that the peak landward wind generates strong inflow through the entire water column over the sill.

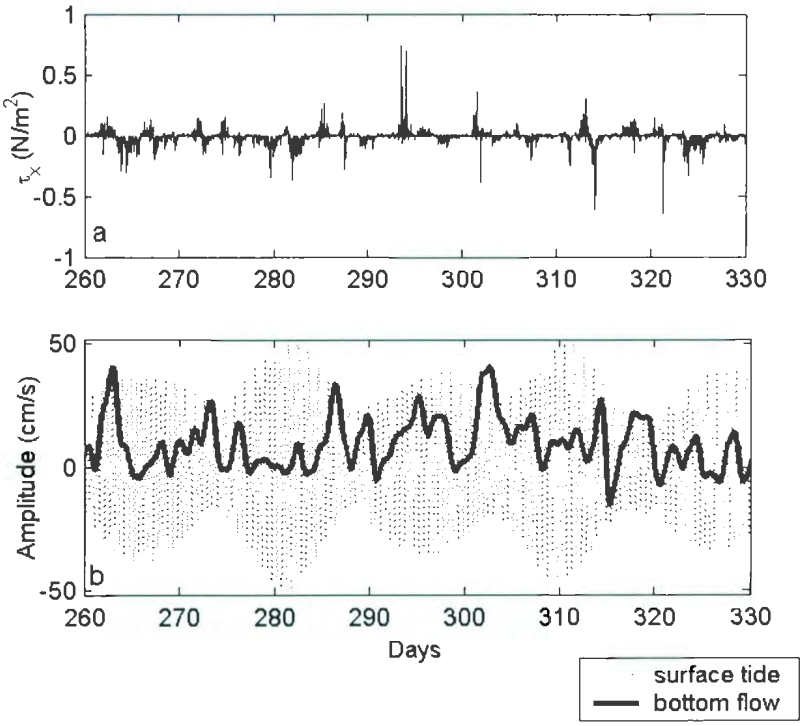

Figure 5.2: Time series of a) alongshore wind stress, b) alongshore velocity amplitude of surface tide with lowpass-filtered bottom flow, between days 260 and 330. (+) denotes landward direction, and (-) denotes seaward direction.

Harmonic analysis is applied to surface horizontal velocity vectors on 7-day segments of data to separate the spring-neap cycles, and then the lowpass filtered bottom velocities are averaged every 7 days at each depth corresponding to the tide segments. The moored ADCP allows calculation of the Eulerian transport over the sill. The bottom volume transport is defined to be the depth-integrated along-channel transport in the deeper layer with the transect area 450 m $\times$ 7 m (width of the transect $\times$ depth of the lower layer, Figure 5.3). A scatter plot is used to determine whether a relationship exists

between the bottom volume transport and tidal amplitude (Figure 5.4). Quantified with a linear regression, the two data sets have a negative correlation: bottom transport increases with decreasing tidal amplitudes, indicating that the enhanced circulations occur during neap tides and augment the deep-water renewal. The transport is found to change by as much as a factor of four between spring and neap tides: the minimum volume transport 8 m^3/s corresponds to the maximum tidal amplitude 27 cm/s, and the maximum transport 45 m^3/s is coincident with the weak tidal amplitude 12 cm/s.

The results presented demonstrate the likely generation mechanisms for the low-frequency non-tidal flow in Bonne Bay fjord; the behaviour of the subtidal circulation responds primarily to the spring-neap cycles but might also be in relation to changes in wind stress and direction. The results are quite different from what Richards (2005) found in his research, but are still considered to be reasonable, because the wind stress is highly variable in both space and time and it is difficult to obtain the exact wind forcing over the sill. Farmer and Smith (1980) also believe that wind forcing does not appear to play a dominant role in the sill dynamics. Their research in Knight Inlet, British Columbia indicates that wind-induced effects, except very close to the surface relative to the pycnocline, are invariably small in comparison to the tidally induced exchanges, in contrast, only strong winds may have a significant influence on the circulation away from the sill, which also has been approved in this research. Variations of hydrographic properties (density or temperature) at the bottom are important to examine the deep-water renewal since the flows have differences in both temperature and density between the

inner basin and outer area. Successive hydrographic data are not available in this research due to several large gaps in this 70 day time series.

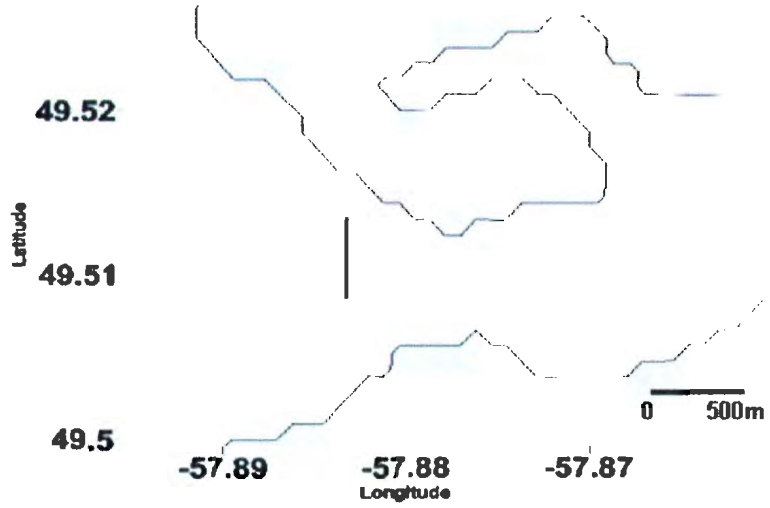

Figure 5.3: Transect across the sill on which the volume transport is calculated.

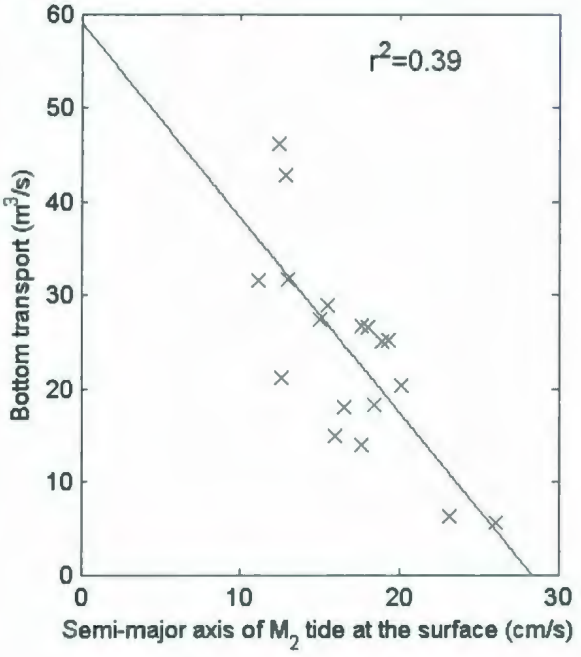

Figure 5.4: Scatter plot of surface tide amplitude (cm/s) and bottom volume transport. The solid line indicates the linear regression, coefficients obtained from least square method. $r^2 = 0.39$.

5.2 High-Frequency Internal Waves

The basic mechanism of high-frequency internal waves is the same as the internal tide since the internal tides are the internal waves at tidal frequencies. Internal waves can be generated by the atmosphere through traveling pressure fields, variable buoyancy flux, variable wind stress, or surface waves (Garrett and Munk 1979). Internal tides belong to the long-period internal waves, whereas the high-frequency internal waves are short-period waves with periods significantly less than 12 hours. It has been reported that the

short-period internal waves can be generated by long-period ones, or are associated with the change of tide cycles (Roberts 1975). This cascading process, from the barotropic tides to the baroclinic components, eventually leads to the transformation of tidal energy into turbulence and heat in the ocean, which has an important role in transportation of marine organism and sediments (Warren et al. 2003).

5.2.1 Basic Dynamics

A brief discussion of the basic fluid-dynamical properties of internal waves is given by Garret and Munk (1979). Describing fluctuations in the ocean related to internal waves involves dispersion and particle motion. In a stratified fluid, the degree of density stratification is quantified by $N^2 = g\rho^{-1}\partial\rho/\partial z$ (profile of N over the sill shown in Figure 3.4). $N(z)$ is the buoyancy frequency with which a vertically displaced fluid element would be expected to oscillate due to the restoring buoyancy forces. The restoring force of the non-vertical displacement becomes less and so the frequency of oscillation is reduced. The dispersion relation is

$$\omega^2 = (N^2k^2 + f^2m^2)/(k^2 + m^2) = N^2\cos^2\theta + f^2\sin^2\theta \qquad (5.1)$$

which connects the frequency ω, horizontal wavenumber k, vertical wavenumber m, and angle to the horizontal θ of the vector wavenumber **K**. Here f is the Coriolis frequency. As indicated in Section 4.2.1, the permissible range of frequencies is $f \le \omega \le N$. The particle motion is almost horizontal and circular when frequencies are slightly greater than f (Figure 5.5a), whereas at higher frequencies, the ellipse becomes more eccentric and inclined to the horizontal, tending to a vertical motion at N (Figure 5.5b). The

velocity vector rotates clockwise in northern hemisphere (anticlockwise in the southern hemisphere when viewed from above).

An important property of the dispersion relation (5.1) is that the frequency ω depends only on the angle of the wave vector **K** = (k, m) to the horizontal, and not on its magnitude (Garret and Munk, 1979). The group velocity is given by

$$(\partial\omega / \partial k, \partial\omega / \partial m) = km\omega^{-1}(N^2 - f^2)(k^2 + m^2)^{-2}(m, -k) \qquad (5.2)$$

which is orthogonal to the direction **K** of wave phase propagation (Figure 5.5). In an incompressible fluid, such as the ocean at internal wave scales, it gives that both **u** and energy flux are perpendicular to **K** (not applicable to all types of wave, Garret and Munk, 1979).

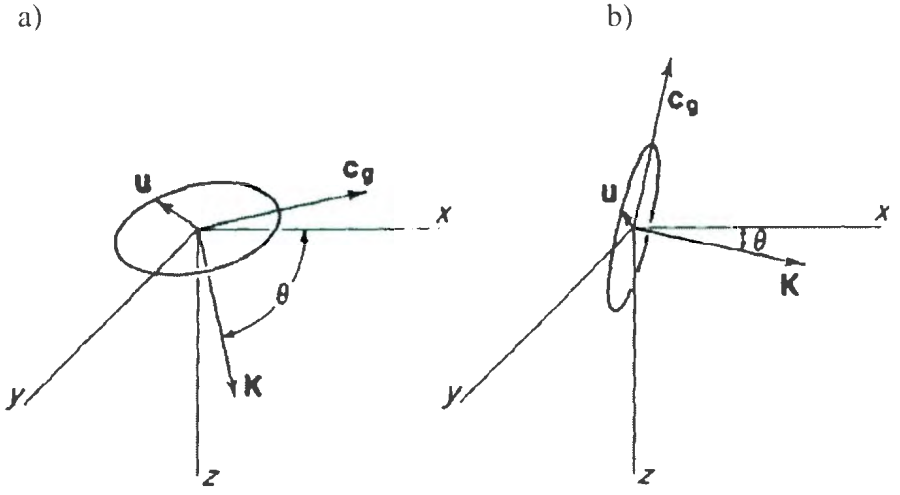

Figure 5.5: The wave vector **K** = (k, m), group velocity c_g , and the hodograph of the particle velocity **u**(t) near, a) inertial frequency, and b) buoyant frequency. **K** is normal to both c_g and **u** (Garrett and Munk, 1979).

5.2.2 Observations

The velocity data with high temporal-resolution in fall and winter, 2006, with 15-min sampling interval compared to coarser resolution, 30-min interval in summer data, provide a more detailed structure of motions over the sill and reveal that in addition to the previously described tidal/subtidal currents, the sill is also an important site for high-frequency internal waves. The Power Spectral Density of alongshore velocity through all the depths presents energetic high-frequency motions with period of 80 minutes (Figure 5.6). Tidal analysis has indicated that M_8 with period of 3 hrs is the tidal constituent with the highest frequency over the sill, the short-period flows therefore are thought to be the high-frequency internal wave, with the ratio of its kinetic energy to the barotropic tides around 1%.

Internal waves have frequently been observed acoustically by high-frequency echo-sounders (Orr et al. 2000; Wiebe et al. 1997; Sandstrom et al. 1989). High-frequency sound (>10 kHz) in the ocean can be scattered by many different sources, including marine organisms, temperature and salinity microstructure, suspended sediments, and air bubbles, which cause difficulties in interpreting the acoustic data. In many cases, turbulence in the water column produces the microstructure with detectable amounts of acoustic backscatter, and the temperature and salinity microstructure associated with the mixing processes are more important in physical oceanography (Woods 1977; Warren et al. 2003). In this research, the highly-resolved acoustic images from multiply-frequency Biosonics echo-sounders allow detailed examination and interpretation of the internal motions associated with tidal flows. Figure 5.8 and 5.9 give

the surface height and acoustic images from three transducers at frequencies of 120 kHz, 220 kHz, and 440 kHz, respectively. It is obvious that high-frequency wave structures develop at the sill only during ebb tide, while reduced high-frequency activity is associated with flood tide. Figure 5.9 shows a more detailed structure of the high-frequency wave during the ebb on day 186: the amplitude of the internal wave is about 3 m and period is around 80 minutes, in agreement with the spectrum plot of Figure 5.6. The group velocity, the velocity with which a packet of internal waves propagates, is given by $c_g = \sqrt{g' h_1 h_2 / (h_1 + h_2)}$ (deYoung and Pond 1989), where h_1 and h_2 are the depths of the upper and lower layers, respectively, and g' is the reduced gravity, $g' = (\rho_2 - \rho_1) g / \rho_2$. Here in Bonne Bay, $h_1 = h_2 = 6$ m and $g' \approx 0.04$ m/s^2, result in group velocity $c_g = 35$ cm/s, at which the energy is conveyed along internal waves.

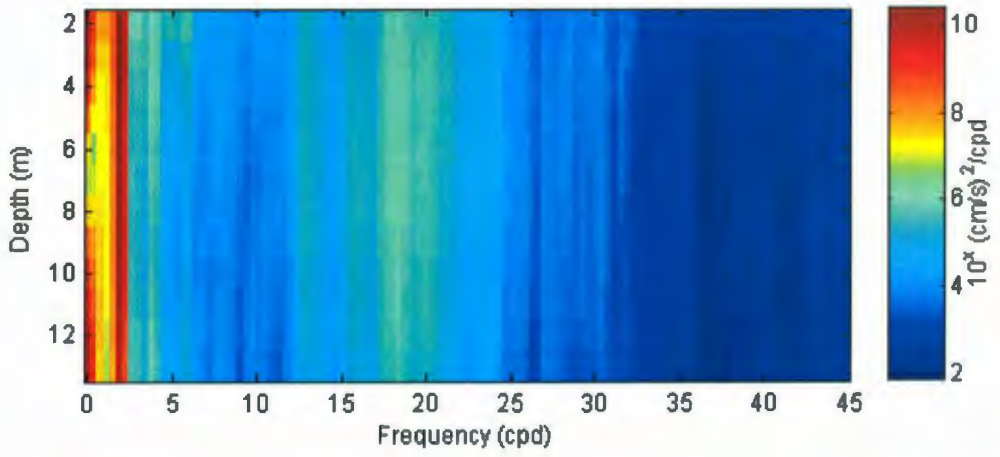

Figure 5.6: Power Spectral Density (PSD) of alongshore velocity at all depths using the BB06_c ADCP data, between September, 2006 and March, 2007. The sampling rate is 15 min. Number of degrees of freedom is 21.

In addition to wave-induced scattering, other isolated patches of strong backscatter (red spots), over -40 dB, can be observed from the acoustic images collected using multi-frequency echosounders (Figure 5.7 bottom, and 5.8), which are seemingly unaffected by the internal waves. The isolated patches are random and rare; whereas the wave-related scattering is prominent at all three frequencies, and hence they are most likely the active swimmers in the ocean, such as fish (Warren et al. 2003). The most intensified backscatter occurs at surface which has the constant volume backscattering values with time, and the surface elevation is extracted according to the level of this maximum backscatter intensity (Figure 5.7 top).

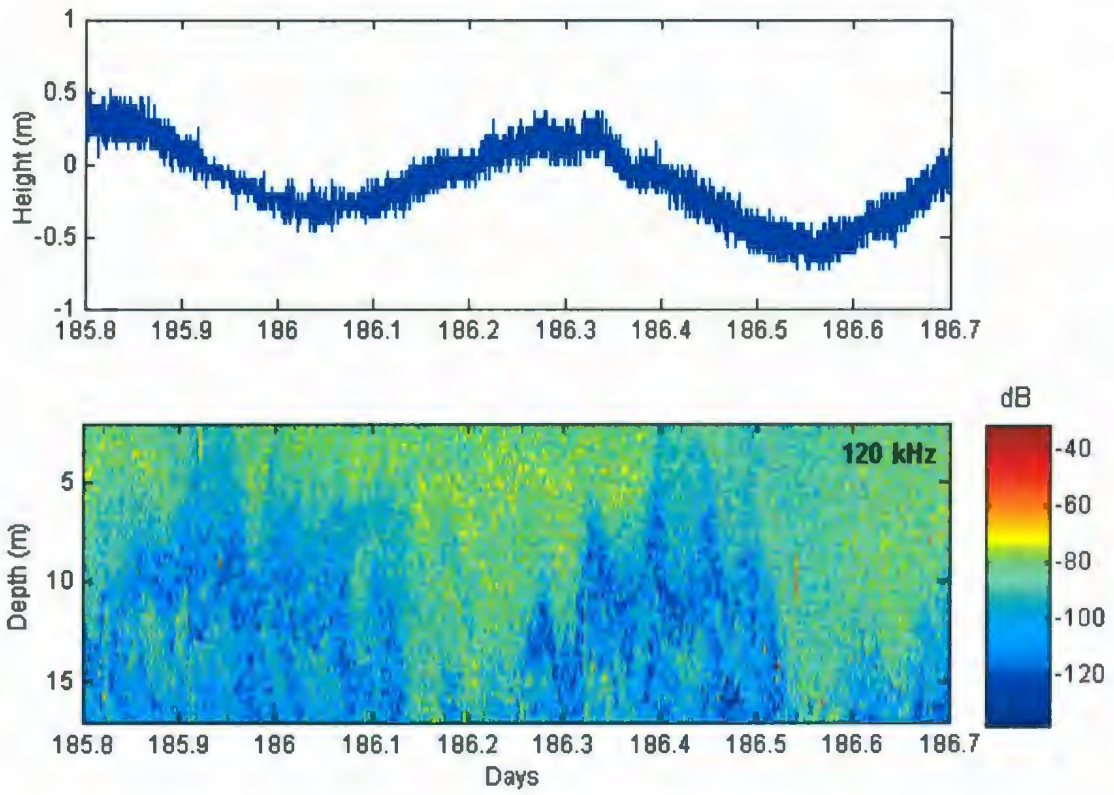

Figure 5.7: Time series of surface height (top) and acoustic backscatter through the whole water column (bottom) collected by 120 kHz Biosonics echo-sounder, between days 185 and 186. The backscatter levels are expressed as volume backscattering strength Sv (dB re m^{-1}).

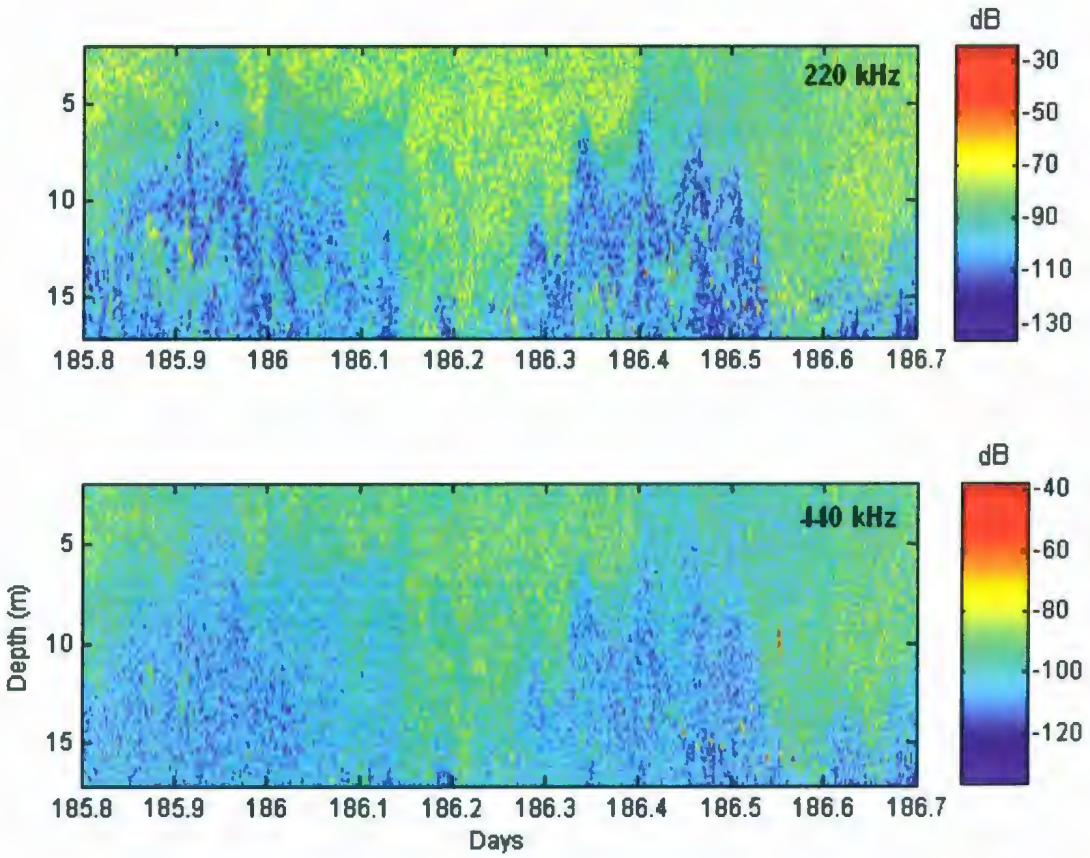

Figure 5.8: Time series of volume backscattering strength collected by the 220 kHz and 440 kHz Biosonics echo-sounders, respectively, between days 185 and 186. The internal waves have different scattering strength at different frequencies.

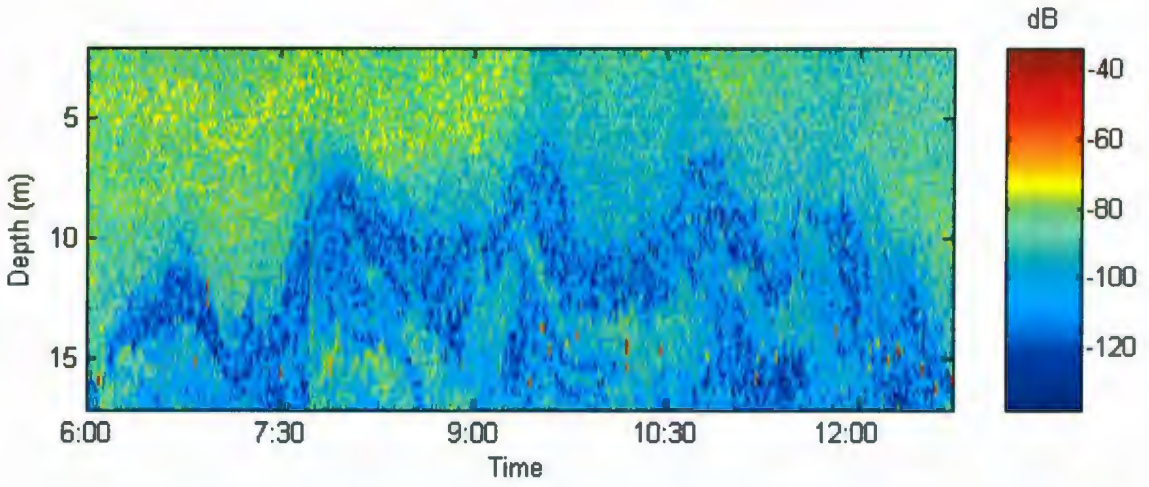

Figure 5.9: Acoustic image during an ebb tide sequence collected by 120 kHz echo-sounder on day 191. The backscatter levels are expressed as volume backscattering strength (Sv).

5.3.3 Interpretation

The asymmetry in the wave occurrence between flood and ebb tides can be explained by the Froude number, $F = U / C$, where U is the magnitude of the depth-averaged alongshore current, C is the propagation speed of the internal waves (Baines 1995; Loder et al. 1992). During strong tidal flow, $U \approx 25$ cm/s, $C \approx 15$ cm/s, yields $F > 1$, which means that sill is a supercritical region during strong tide when tide is sufficient magnitude to prevent internal waves from propagating over the sill. During weak tides, the Froude number is significantly less than 1, and the sill remains subcritical with a strong stratification, in which case the interfacial wave is allowed.

Question arises about where the internal waves are generated. Figure 5.7 shows that the high-frequency internal wave is generated during ebb tide, which indicates that internal waves propagate with the outflowing tide, and the direction the wave propagation is from right to left, from the inner basin to the outer area. Figure 5.10 shows a wave structure with the corresponding alongshore and vertical velocities. Farmer and Smith (1980) have observed that well-defined trains of lee waves can be generated on the lee side of the sill during a moderate ebb tide and propagate over the sill with the ebb in strongly stratified summer conditions and even in November, at Knight Inlet, British Columbia. The research conducted by Loder et al. (1992) on Georges Bank indicates that internal waves generated over the bank side can not move onto the bank during strong off-bank flow, but can be advected onto the bank during on-bank flow. In Bonne Bay, the internal wave propagates from the inland side of the sill toward ocean with the ebb, and the mechanism of the internal motions is suspected to be that the high-frequency waves generated during the ebb on the lee side of the sill and then propagate over the sill with the ebb tide.

The most likely way for internal waves to dissipate is by the occasional Kelvin-Helmholtz shear instability due to the random superposition of different internal waves bringing the local Richardson number $Ri = N^2 / (du/dz)^2$ down below the critical value of 0.25 (Garret and Munk 1979). When Ri is small, typically considered below 1/4, velocity shear is considered sufficient to overcome the stratification, and some mixing will generally occur. When Ri is large, the stratification remains stable and turbulent mixing across the stratification is generally suppressed. Using Ri to investigate mixing

and stratification, however, is not applicable to the data set in Bonne Bay because during either strong or weak tidal period, Ri always has values much larger than unity at any depth of water column, which theoretically means that turbulence never exists over the sill. This is unlikely to be true in general because turbulence will surely occur during strong tidal flows over the sill, and they can also be generated with internal wave propagation.

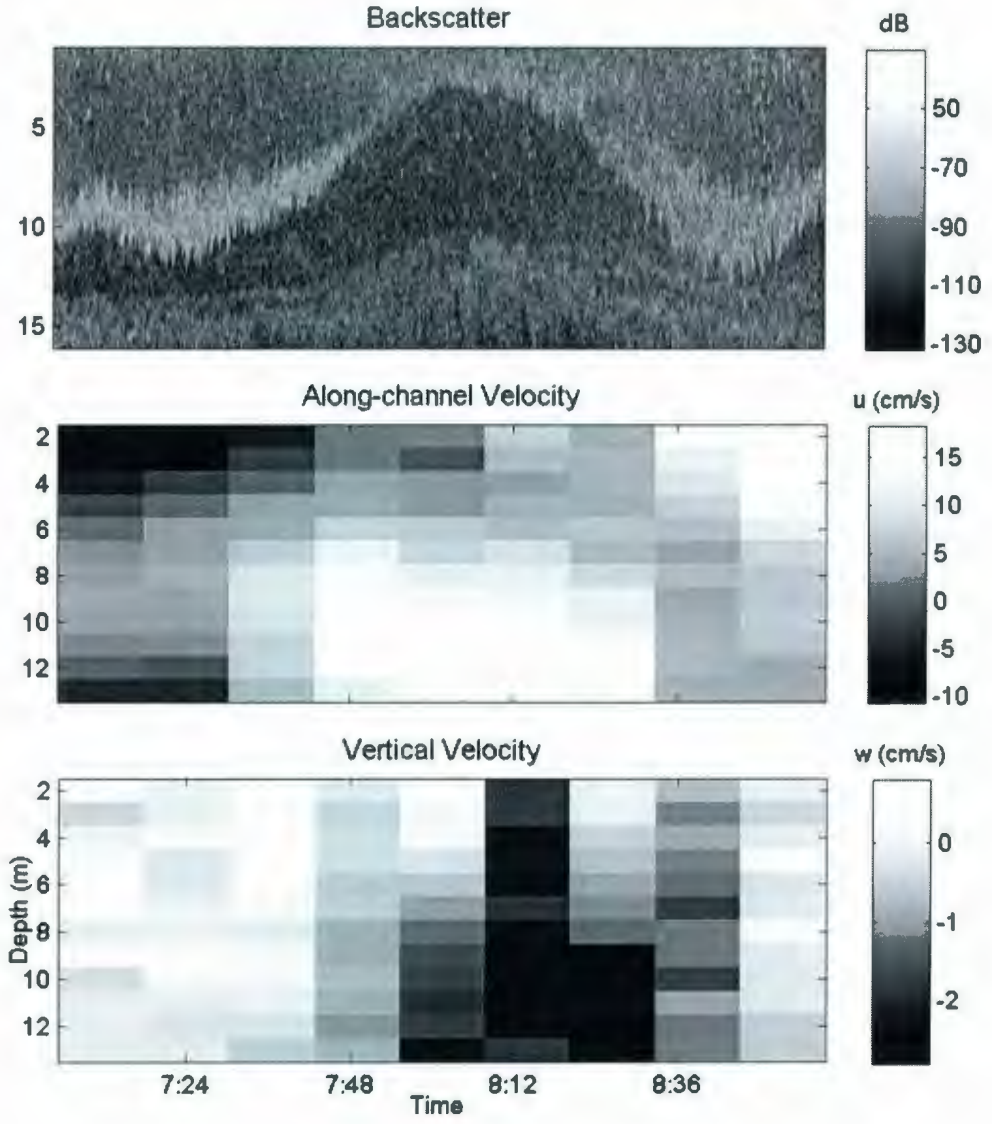

Figure 5.10: Time series of acoustic backscatter, alongshore velocity, and vertical velocity. Acoustic backscatter is measured with the 120 kHz echo sounder. (+) in the vertical velocity means upward direction, (-) is the downward direction. The direction of wave propagation is to the left.

6 Conclusions

6.1 Thesis Results

The temporal variability of the circulation and exchange process over the Bonne Bay sill has been observed by moored current meters and hydrographic instruments. The dynamics at different time scale have been presented. Generally flow over the sill has a steady two-layer circulation system, with outflow in the upper layer and inflow in the deeper layer throughout the whole sampling time. The position of the intermediate layer is near the center of the water column and has temporal variability with seasons due to the variations of freshwater input and wind forcing.

The observations in year 2006 indicate that tides seem to be the dominant forcing for the flow over the sill and that there is an energetic interaction between the stratified water driven by tidal current and the sill during the sampling time. The M_2 tide is the most energetic tidal constituent and contributes 70% of the total tidal kinetic energy. It has an amplitude four times larger than the next largest constituent S_2 and seven times larger than K_1. Semidiurnal baroclinic signals can only be detected in summer time, when there is strong stratification over the sill. In fall and winter, flows are found to be most nearly barotropic due to the weakly stratified water. The semidiurnal internal tide has a vertical structure dominated by mode-1, with amplitudes intensified at both surface and bottom, and travels with the phase velocity of 16 cm/s and wavelength of 7 km, and contains 20% of the surface tidal energy. No diurnal internal tides have been observed over the sill throughout the year due to their weak amplitudes (the K_1 constituent contains

around 4% of the M_2 kinetic energy), and the driving force is not strong enough to generate diurnal internal tides.

The current meter data set that cover 70 days in fall, when the freshwater input is approximately constant (Richards, 2005), show evidence that the spring-neap tidal variability of the turbulent mixing modulates the strength of the low-frequency circulation associated with the deep water renewal, with maximum volume transport at the bottom occurring during neap tides compared to insignificant exchange processes at springs. The phenomenon illustrates the dependence of subtidal currents on tidal amplitude and suggests that the dominant mechanism for generating low-frequency exchange events is the baroclinic forcing driven by horizontal density gradient instead of wind forcing. Only peak wind has an additional effect on the flow.

In addition to tidal and subtidal currents, the high-frequency internal waves with period of 80 mins have also been identified in the data set from the current meter with a higher temporal resolution. The interesting characteristic of the internal wave is its asymmetry during the tidal cycles: they are only generated during ebb tide, with small amplitude, around 3 m, and group velocity 35 cm/s. The ratio of its kinetic energy to the barotropic tides is 1%. The high-frequency internal waves are generated near the side of the inner basin and propagate towards the outer area.

6.2 Future Work

The studies in Bonne Bay have investigated many aspects of flows over the sill, but there are still questions unsolved and more observations and analysis are needed to deal with the details of the dynamics. So far, it is hard to distinguish whether the internal

tides are generated locally at the sill, or propagated there from a generation site outside the bay, or consist of some combination of the two. The topography of Bonne Bay (Figure 2.1) somehow indicates that the possible regions for baroclinic tides could be over the sill, or the shelf along the South Arm. The shelf of the South Arm however has depths of several meters, which is too shallow to support internal tides. The site for baroclinic tide generation is therefore considered at the sill.

Variations of hydrographic properties are important to examine the deep-water renewal, but are unavailable in this research due to large gaps between the time series. In future work, we expect successive hydrographic sampling, together with current meter data and BioSonics data, with high resolutions in both space and time, to approve the mechanisms about the deep-water renewal and internal waves presented and to examine the connections between waves, fine structure, and turbulence.

Another limitation is the fact that the multiple-frequency echosounder techniques have not been fully used in this research. The characteristics of the scattering involving both physical and biological processes have not been exploited when more than one frequency exists. Theoretical models of acoustic-scattering spectra from biological and physical-scattering processes have different shapes, and these differences make it possible for a multiple-frequency acoustic system in a field survey to differentiate and measure the scattering contributions from these two processes (Warren et al. 2003). The design of any future sampling will depend upon the physical or biological processes that are to be studied.

References

Baines, P. G. (1974). The generation of internal tides over steep continental slopes. *Philosophical Transactions of the Royal Society of London. Series A. Mathematical and Physical Sciences, Vol. 277, No. 1263*, 27-58.

Baines, P. G. (1986). Internal tides, internal waves, and near-inertial motions. In Mooers, C. N., editor, *Baroclinic processes on continental shelves, volume 3* of *American Geophysical Union Coastal and Estuarine Sciences Series, chapter 2*, 19–31. American Geophysical Union, Washington.

Baines, P. G. (1995). *Topographic effects in stratified flows*. Cambridge University Press. 1st edition.

BioSonics Inc. (2002). *BioSonics X-Series echosounder and visual acquisition 5.0 USER GUIDE*. BioSonics Inc, Seattle, WA.

Bourgault, D., M. D. Blokhina, R. Mirshak and D. E. Kelley (2007). Evolution of a shoaling internal solitary wavetrain. *Geophys. Res. Let., 34*, L03601, doi: 10.1029 /2006GL028462.

Chiswell, S. M. and M. Moore (1998). Internal tides near the Kermadec Ridge. *J. Phys. Oceanogr., 29*, 1019-1035.

Clay, C. and H. Medwin (1977). *Acoustical oceanography: principles and applications*. Ocean engineering. A Wiley Series. A WILEY-INTERSCIENCE PUBLICATION. New York.

Comeau, M., G. Y. Conan, F. Maynou, G. Robichaud, J. Therriault and M. Starr (1998). Growth, spatial distribution, and abundance of benthic stages of the snow crab *(Chionoecetes opilio)* in Bonne Bay, Newfoundland, Canada. *Can. J. Fish. Aquat. Sci. 55(1)*, 262–279.

deYoung, B., K. M. Brown, R. S. Adams and S. D. McLean (2005). Design and deployment of the Bonne Bay observatory (B2O). *Oceans 2005, Vol. 1*, 855- 860.

deYoung, B. and S. Pond (1988). The deepwater exchange cycle in Indian Arm, British Columbia. *Estuarine, Coastal and Shelf Science, 26*, 285-308.

deYoung, B. and S. Pond (1989). A partition of the energy loss from the barotropic tide in fjords. *J. Phys. Oceanogr.*, *19*, 246-252.

deYoung, B. and S. Pond (1987). The internal tide and resonance in Indian Arm. *J. Geophy. Res. 92*, 5191-5207.

Deines, K. L. (1999). Backscatter estimation using broadband acoustic Doppler current profilers. In Proc. of *IEEE 6th working conference on current measurement*, 249–253, San Diego, CA.

Dushaw, B. D., B. D. Cornuelle, P. F. Worcester, B. M. Howe and D. S. Luther (1995). Barotropic and baroclinic tides in the central North Pacific Ocean determined from long-range reciprocal acoustic transmission. *J. Phys. Oceanogr.*, *25*, 631-647.

Dyer, K. R. (1997). *Estuaries: a physical introduction.* John Wiley & Sons Ltd, Chichester, 2nd edition.

Ehrenberg, J. E. and T. C. Torkelson (1996). Application of dual-beam and split-beam target tracking in fisheries acoustics. *ICES Journal of Marine Science. 53*, 329–334.

Emery, W. J. and R. E. Thomson (1998). *Data analysis methods in physical oceanography*. Elsevier Science Ltd., 1st edition.

Ennis, G. P., R. G. Hooper and D. M. Taylor (1990). Changes in the composition of snow crab (*Chionoecetes opilio*) participating in the annual breeding migration in Bonne Bay, Newfoundland. *Can. J. Fish. Aquat. Sci. 47(11)*, 2242-2249.

Erofeeva, S. Y., G. D. Egbert and P. M. Kosro (2003). Tidal currents on the central Oregon shelf: models, data and assimilation. *J. Geophys. Res., Vol 108, No. C5*, 3148-3172.

Farmer, D. M. and L. Armi (1999). Stratified flow over topography: the role of small-scale entrainment and mixing in flow establishment. *Proc. R. Soc. Lond. A. 455*, 3221-3258.

Farmer, D. M. and H. J. Freeland (1983). The physical oceanography of fjords. *Progress Oceanography, 12*, 147–220.

Farmer, D. M. and T. R. Osborn (1976). The influence of wind on the surface layer of a stratified inlet. Part 1. Observations. *J. Phys. Oceanogr., 6*, 931-940.

Farmer, D. M. and J. D. Smith (1980). Tidal interaction of stratified flow with a sill in Knight Inlet. *Deep-Sea Research, Vol. 27A*, 239-254.

Foreman, M.G.G. (1977). Manual for Tidal Heights Analysis and Prediction, *Pacific Marine Science Report 78-6*, Institute of Ocean Sciences, Patricia Bay, Victoria, B.C.

Freeland, H. J. and D. M. Farmer (1980). Circulation and energetics of a deep, strongly stratified inlet. *Can. J. Fish. Aquatic Sci., 37,* 1398-1410.

Garrett, C. and W. Munk (1979). Internal waves in the ocean. *Ann. Rev. Fluid Mech., 11,* 339-369.

Geyer, W. R. and G. A. Cannon (1982). Sill process related to deep water renewal in a fjord. *J. Geophys. Res., Vol 87, No. C10,* 7985-7996.

Geyer, W. R., J. H. Trowbridge and M. M. Bowen (2000). The dynamics of a partially mixed estuary. *J. Phys. Oceanogr., 30,* 2035-2048.

Gilbert, D. and B. Pettigrew (1993). Current-meter data from Bonne Bay, Newfoundland, during the summer of 1991. *Canadian Data Report of Hydrography and Ocean Sciences 122.*

Hendry, R. M. (1977). Observations of the semidiurnal internal tide in the western North Atlantic Ocean. *Philosophical Transactions of the Royal Society of London. Series A, Mathematical and Physical Science, Vol 286, No. 1330,* 1-24.

Holloway, P. E. (1984). On the semidiurnal internal tide at the shelf-break region on the Australian north west shelf. *J. Phys. Oceanogr., 14,* 1787-1799.

Holloway, P. E., P. G. Chatwin and P. Craig (2001). Internal tide observations from the Australian north west shelf in summer 1995. *J. Phys. Oceanogr., 31,* 1182-1199.

Inall, M., F. Cottier, C. Griffiths and T. Rippeth (2004). Sill dynamics and energy transformation in a jet fjord. *Ocean Dynamics, 54,* 307-314.

Kang, S. K., M. G. G. Foreman, W. R. Crawford and J. Y. Cherniawsky (2000). Numerical modeling of internal tide generation along the Hawaiian Ridge. *J. Phys. Oceanogr., 31,* 1083-1098.

Klymak, J. M. and M. C. Gregg (2003). Tidally generated turbulence over the Knight Inlet sill. *J. Phys. Oceanogr., 34,* 1135-1151.

Kundu, P. K. and I. M. Cohen (2004). *Fluid Mechanics.* Elsevier Academic Press. Third Edition.

Kurapov, A. L., G. D. Egbert, J. S. Allen, R. N. Miller, S. Y. Erofeeva and P. M. Kosro (2003). The M2 internal tide off Oregon: inferences from data assimilation. *J. Phys. Oceanogr.*, *33*, 1733-1757.

Large, W. G. and S. Pond (1981). Open ocean momentum flux measurements in moderate to spring winds. *J. Phys. Oceanogr.*, *11*, 324-336.

Lerczak, J. A., C. D. Winant and M. C. Hendershott (2003). Observations of the semidiurnal internal tide on the southern California slope and shelf. *J. Geophys. Res.*, *Vol. 108, No. C3*, 3068-3089.

Lorder, J. W., D. Brickman and E. P. W. Horne (1992). Detailed structure of currents and hydrography on the northern side of Georges Bank. *J. Geophys. Res., Vol 97, No. C9*, 14331-14351.

Lorke, A., D. F. McGinnis et. al. (2004). Acoustic observations of zooplankton in lakes using a Doppler current profiler. *Freshwater Biology*, *49*, 1280-1292.

Martec Limited (1982). *Internal Wave Activity at Tidal Frequency on the Labrador Shelf.* Martec Limited, Halifax, Canada.

Medwin, H. et. al. (2005). *Sounds in the sea: from ocean acoustics to acoustical oceanography.* Cambridge University Press. UK.

Miropol'sky, Y. Z. and O. D. Shishkina (2001). *Dynamics of internal gravity waves in the ocean.* Kluwer Academic Publishers, The Netherlands.

Monismith, S. G., J. Burau and M. Stacey (1996). Stratification dynamics and gravitational circulation in Northern San Francisco Bay. in *San Francisco Bay: The Ecosystem*, ed. T. Hollibaugh, 123-153.

Moum, J. N., D. M. Farmer, W. D. Smyth, L. Armi and S. Vagle (2003). Structure and generation of turbulence at interfaces strained by internal solitary waves propagating shoreward over the continental shelf. *J. Phys. Oceanogr., 33*, 2093-2112.

Munk, W., F. Snodgrass and M. Wimbush (1970). Tides off shore: Transition from California coastal to deep-sea waters. *Geophys. Fluid Dyn., 1,* 161-235

Nash, J. D., E. Kunze, C. M. Lee and T. B. Sanford (2006). Structure of the baroclinic tide generated at Kaena Ridge, Hawaii. *J. Phys. Oceanogr., 26*, 1123-1135.

Odamaki, M (1994). Tides and tidal current along the Okhotsk coast of Hokkaido. *J. Phys. Oceanogr., 50,* 265-279.

Orr, M. H., L. R. Haury, P. H. Wiebe and M. G. Briscoe (2000). Backscatter of high-frequency (200 kHz) acoustic wavefields from ocean turbulence. *J. Acoust. Soc. Am. 108(4),* 1595-1601.

Pawlowicz, R., B. Beardsley and S. Lentz (2002). Classical tidal harmonic analysis including error estimates in MATLAB using T_TIDE. *Computers and Geosciences 28,* 929-937.

Petruncio, E. T., L. K. Rosenfeld and J. D. Paduan (1998). Observations of the internal tide in Monterey Canyon. *J. Phys. Oceanogr., 28,* 1873-1903.

Pickard, G. L. and W. J. Emery (1990). *Descriptive physical oceanography*: Butterworth-Heinemann, 5th edition.

Pond, S. and G. L. Pickard (1983). *Introductory dynamical oceanography*. Butterworth-Heinemann, 2nd edition.

Ray, R. D. and G. R. Mitchum (1996). Surface manifestation of internal tides generated near Hawaii. *Geophys. Res. Let., Vol.23. No. 16,* 2101-2104.

Ribeiro, C. H. A., J. J. Waniek and J. Sharples (2004). Observations of the spring-neap modulation of the gravitational circulation in a partially mixed estuary. *Ocean Dynamics, Vol. 54, Issue 3-4,* 299-306.

Richards, C. and B. deYoung (2004). *Analysis of physical oceanographic data from Bonne Bay, September 2002 - September 2004.* Physics and Physical Oceanography Data Report 2004-1, Department of Physics and Physical Oceanography, Memorial University of Newfoundland.

Richards, C. (2005). *Wind-forced dynamics in Bonne Bay, Newfoundland.* M.Sc thesis, Department of Physics and Physical Oceanography, Memorial University of Newfoundland.

RD Instruments (1996). *Acoustic Doppler current profiler principles of operation: a practical primer.* RD Instruments, San Diego, CA.

Roberts, J. (1975). *Internal gravity waves in the ocean. Marine Series Vol. 2.* Marcel Dekker, Inc., New York.

Sandstrom, H. and N. S. Oakey (1994). Dissipation in internal tides and solitary waves. *J. Phys. Oceanogr., 25,* 604-614.

Sandstrom, H., J. A. Elliott and N. A. Cochrane (1989). Observing groups of solitary internal waves and turbulence with BATFISH and Echo-Sounder. *J. Phys. Oceanogr., 19,* 987-997.

Satlantic Inc. (2006). *System design description, Bonne Bay Observatory,* Satlantic Inc, Halifax, Nova Scotia, Canada.

Seabird Electronics, Inc (2004). *SBE 19plus SEACAT PROFILER user manual, version 012,* Seabird Electronics, Inc. Washington, US.

Seim, H. E., M. C. Gregg and R. T. Miyamoto (1995). Acoustic backscatter from turbulent microstructure. *Journal of Atmospheric and Oceanic Technology, Vol. 12,* 367-380.

Simmonds, E. J., N. J. Williamson, G. Gerlotto and S. Aglen (1992). Acoustic survey design and analysis procedure: A comprehensive review of current practice, ICES Copenhagen, Denmark, *ICES Cooperative Research Rep. No.187.*

Stacey, M. W. and L. J. Zedel (1986). The time dependent, hydraulic flow over the sill of Observatory Inlet. *J. Phys. Oceanogr., 16,* 1062-1076.

Stigebrandt, A. (1999). Evidence for baroclinic wave drag in fjords. In: Muller P, Henderson D (eds) *Dynamics of oceanic internal gravity waves II. SOEST Special Production,* 73-82.

Tian, R., A. F. Vezina, M. Starr and F. Saucier (2001). Seasonal dynamics of coastal ecosystems and export production at high latitudes: a modeling study. *Limnology and Oceanography, 46(8),* 1845-1859.

Valle-Levinson, A. and L. Atkinson (1999). Spatial gradients in the flow over an estuarine channel. *Estuaries, 22(2A),* 179-193.

Warren, J. D., T. K. Stanton, P. H. Wiebe and H. E. Seim (2003). Inference of biological and physical parameters in an internal wave using multiple-frequency, acoustic-scattering data. *ICES Journal of Marine Science, 60,* 1033-1046.

Webb, A. J., and S. Pond (1986). A modal decomposition of the internal tide in a deep, strongly stratified inlet: Knight Inlet, British Columbia. *J. Geophys. Res., 91,* 9721-9738.

Wiebe, P. H., and T. K. Stanton et. al. (1997). High-frequency acoustic volume backscattering in the Georges Bank coastal region and its interpretation using scattering models. *IEEE. Journal of oceanic engineering, Vol. 22, No. 3,* 445-464.

Woods, J. D. (1977). Turbulence as a factor in sound scattering in the upper ocean. *Oceanic Sound Scattering Prediction,* 129-145. Ed. By N. R. Andersen, and B. J. Zahurance. Plenum Press, New York.

Wunsch, C. (1975). Internal tides in the ocean. *Reviews of Geophysics and Space Physics, Vol. 13, No. 1,* 167-182.